THE JOURNAL OF PHYSICAL CHEMISTRY A

Article

Novel TiO/CN Photocatalysts for Photocatalytic Reduction of CO and for Photocatalytic Decomposition of NO

Martin Reli, Pengwei Huo, Marcel Šihor, Nela Ambrožová, Ivana Troppová, Lenka Mat#jová, Jaroslav Lang, Ladislav Svoboda, Piotr Ku#trowski, Michal Ritz, Petr Praus, and Kamila Ko#í

J. Phys. Chem. A, **Just Accepted Manuscript** • DOI: 10.1021/acs.jpca.6b07236 • Publication Date (Web): 05 Oct 2016

Novel TiO_2/C_3N_4 Photocatalysts for Photocatalytic Reduction of CO_2 and for Photocatalytic Decomposition of N_2O

Martin Reli[1], Pengwei Huo[1], Marcel Šihor[1], Nela Ambrožová[1], Ivana Troppová[1], Lenka Matějová[1], Jaroslav Lang[1], Ladislav Svoboda[1,2], Piotr Kuśtrowski[4], Michal Ritz[2], Petr Praus[1,2], Kamila Kočí[1,3]*

1 Institute of Environmental Technology, 2 Department of Chemistry, 3 Centre ENET, VŠB-TU Ostrava, 17. listopadu 15/2172, 708 33 Ostrava, Czech Republic

4 Faculty of Chemistry, Jagiellonian University in Kraków, ul. Ingardena 3, 30-060 Kraków, Poland

Abstract

TiO_2/g-C_3N_4 photocatalysts with the ratio of TiO_2 to g-C_3N_4 ranging from 0.3/1 to 2/1 were prepared by simple mechanical mixing of pure g-C_3N_4 and commercial TiO_2 Evonik P25. All the nanocomposites were characterized by X-ray powder diffraction, UV-vis diffuse reflectance spectroscopy, photoluminescence, X-ray photoelectron spectroscopy, Raman spectroscopy, infrared spectroscopy, transmission electron microscopy, photoelectrochemical measurements and nitrogen physisorption. The prepared mixtures along with pure TiO_2 and g-C_3N_4 were tested for the photocatalytic reduction of carbon dioxide and photocatalytic decomposition of nitrous

oxide. The pure g-C_3N_4 exhibited the lowest photocatalytic activity in both cases pointing to a very high recombination rate of charge carriers. On the other hand, the most active photocatalyst towards all the products was (0.3/1)TiO_2/g-C_3N_4. The highest activity is achieved by combination of number of factors: (i) specific surface area, (ii) adsorption edge energy, (iii) crystallite size and (iv) efficient separation of the charge carriers. Where the efficient charge separation is the most decisive parameter.

1. Introduction

The greenhouse effect and global warming are the most discussed topics of present days. A number of initiatives is trying to come up with a way how to decrease emissions of greenhouse gases. CO_2, CH_4, N_2O and fluorinated gases belong among anthropogenic greenhouse gases. Carbon dioxide and nitrous oxide is one of the highest contributors to global warming based on their radiative forcing and concentration at the atmosphere [1].

Carbon dioxide's radiative forcing is around 1.74 W m^{-2} and it is estimated CO_2 is the largest contributor in global warming accounting for 63 % of total radiative forcing [2]. Carbon dioxide is mainly produced from fossil fuels combustion and it is estimated more than 31 billion tons of CO_2 is produced annually all over the world [3]. The CO_2 concentration in the atmosphere already crossed 400 ppm in most places and keeps increasing approximately about 2 ppm per year [4]. One of the closely watched methods how to utilize carbon dioxide is its photocatalytic reduction. The reaction is mostly done under UV irradiation and the reaction scheme is as follows:

$$CO_2 + H_2O \xrightarrow{hv,photocatalyst} Carbonaceous\ products + O_2 \qquad (1)$$

Nitrous oxide is the third highest contributor to global warming, accounting approximately for 6.2 % of global radiative forcing. The concentration of N_2O at the atmosphere is quite low

(320 ppb) but its contribution to global warming potential is nearly 300 times higher than the one of CO_2 [1]. The photoinduced decomposition is focused on both indoor and outdoor abatement of nitrous oxide. The reaction is carried out under ambient conditions and UV or visible irradiation as:

$$N_2O \xrightarrow{hv,photocatalyst} N_2 + \frac{1}{2}O_2 \quad (2)$$

The photocatalytic reduction of carbon dioxide attracted great attention after the successful photoelectrocatalytic reduction of CO_2 by Innue et al. [5]. Since then the number of publication focusing on the photocatalytic reduction of CO_2 rises exponentially every year. Due to high attention of this topic there are several thorough reviews summing up the state of art [6-9]. Nitrous oxide on the other hand is attracting only partial attention of the photocatalytic society and to the best of authors´ knowledge there are no reviews summarizing achievements in the field of photocatalytic reduction of nitrous oxide. Matsuoka et al. conducted the photocatalytic reduction of N_2O in the presence of zeolite photocatalysts in the beginning of this millennia [10, 11] but after that there have not been reported any papers dealing with photocatalytic reduction of nitrous oxide. Our group published several papers about photocatalytic reduction of N_2O in the presence of ZnS immobilized on montmorillonite and TiO_2 based photocatalysts [12-14].

The most studied photocatalyst is, without any doubt, titanium dioxide. Nevertheless, carbon nitride has attracted huge attention in last couple years. Especially graphitic carbon nitride (g-C_3N_4) has been used as photocatalyst quite extensively. The g-C_3N_4 is one of materials with medium sized band gap (2.7 – 2.8 eV) capable of visible light absorption. It is also relatively chemically, photochemically and thermally stable semiconductor. The main drawback of g-C_3N_4 is its high recombination rate of generated charge carriers which is resulting in low photocatalytic performance. The extensive review of g-C_3N_4 of Dong et al. summarizes its

properties and utilization as photocatalyst [15]. The review of Ye et al. goes even further and summarizes the fabrication methods of C_3N_4 and its utilization for photocatalytic water splitting and CO_2 reduction [16].

In order to slow down the recombination rate of charge carriers the creation of heterojunction on the semiconductor's surface has been studied. Various different heterojunctions have been studied and tested to improve the photocatalytic activity of g-C_3N_4 [17-19]. Yu et al. successfully prepared ZnO/g-C_3N_4 heterostructure and used it for the photocatalytic reduction of carbon dioxide and obtained results twice higher than in the presence of pure ZnO or g-C_3N_4 [20]. Although there are many possibilities for creating the heterostructure the TiO_2/g-C_3N_4 is one of the most extensively studied one. There have been many studies focused on TiO_2/g-C_3N_4 for its superior visible light absorption [21-33]. The most of the mentioned studies tested the photocatalytic activity of the TiO_2/g-C_3N_4 composite on degradation of organic pollutants in liquid phase. This work was focused on testing the photocatalytic activity of mechanically created mixtures of TiO_2 and g-C_3N_4 for two different reactions, the photocatalytic reduction of CO_2 and photocatalytic reduction of N_2O, respectively.

2. Experimental

2.1. Preparation of TiO_2/g-C_3N_4 photocatalysts

The g-C_3N_4 was synthesized by simple heating of melamine in the muffle furnace. 10 g of melamine powder as precursor were heated to 550 °C at a heating rate of 10 °C/min in a covered crucible. The temperature was kept at 550 °C for 2 h and then cooled down to room temperature. A yellow product of g-C_3N_4 was obtained and was ground to a fine powder.

As a precursor of TiO_2 commercial P25 (Evonik) was used. The TiO_2/g-C_3N_4 composites were prepared by mechanical mixture and calcined in a muffle furnace at 450 °C for 2 h with

temperature increasing at the rate of 10 °C/min. The samples were labelled according to weight ratio of TiO_2/g-C_3N_4 as follows: (0.3/1), (0.5/1), (1/1) and (2/1) TiO_2/g-C_3N_4.

2.2. Characterization of photocatalysts

X-ray powder diffraction patterns (XRD) were measured using a Bruker D8 (Bruker AXS) diffractometer equipped by a detector sensitive for the placement (VÅNTEC 1). The CoKα lamp was used as a source of irradiation of wavelength λ = 0.178897 nm. Measurements were done in the conventional Bragg–Brentano setup.

Nitrogen physisorption at 77 K was performed on a 3Flex automated volumetric apparatus (Micromeritics Instruments, USA) after degassing of materials at 150 °C for more than 24 h under vacuum below 1 Torr. Degassing at low temperature was applied to remove physisorbed water, but having no influence on the porous morphology of the developed materials. The specific surface area was calculated according to the classical Brunauer–Emmett–Teller (BET) theory for the p/p0 range of 0.05–0.30 [34]. As the specific surface area, S_{BET}, is not a proper parameter in the case of mesoporous solids containing micropores [35], the mesopore surface area, S_{meso}, and the micropore volume, V_{micro}, were also evaluated based on the *t*-plot method [36] with the C_{modif} constant [35, 37]. The net pore volume, V_{net}, was determined from the nitrogen adsorption isotherm at maximum p/p0 (~0.99). The pore-size distribution was evaluated from the adsorption branch of the nitrogen adsorption desorption isotherm by the Barrett–Joyner–Halenda (BJH) method [38] using the de Boer standard isotherm and assuming cylindrical pore geometry.

IR spectra of samples were measured by potassium bromide pellets technique. Exactly 1.0 mg of sample was ground with 200 mg dried potassium bromide. This mixture was used to prepare the potassium bromide pellets. The pellets were pressed by 8 tons for 30 seconds under vacuum. The IR spectra were collected using FT-IR spectrometer Nexus 470 (ThermoScientific, USA)

with DTGS detector. The measurement parameters were the following: the spectral region of 4000-400 cm^{-1}, spectral resolution 4 cm^{-1}; 64 scans; the Happ-Genzel apodization. Treatment of spectra: polynomial (second order) baseline, subtraction spectrum of pure potassium bromide.

A 180° sampling was used as measurement technique of Raman spectroscopy. The Raman spectra were measured at dispersive Raman spectrometer DXR SmartRaman (ThermoScientific, USA) with CCD detector. The measurement parameters were as follows: excitation laser 780 nm, grating 400 lines/mm, aperture 50 μm, exposure time 1 second, number of exposures 1000, the spectral region of 1800-50 cm^{-1}. An empty sample compartment was used for background measurement. Treatment of spectra: fluorescence correction (6^{th} order).

The UV–visible spectra of prepared nanocomposites were recorded using a UV-2600 spectrophotometer with an ISR-2600 integrating sphere attachment (Shimadzu Scientific Co., Japan) from 220 to 1400 nm. Sampling interval was 1 nm and width of slit was 2 nm. Barium sulphate ($BaSO_4$) was used as reference material.

Photoluminescence (PL) spectra were measured by a spectrometer FLS920 (Edinburgh Instrument Ltd, UK). The spectrometer was equipped with a 450 W Xenon lamp (Xe900). The excitation wavelength was 325 nm. The width of excitation and emission slits was 0.5 nm.

Gas chromatography with isotope ratio mass spectrometry (GC/IRMS) DELTA Advantage (Thermo Scientific, USA) was used for the detection of ^{13}C in gas samples before and after photocatalytic reaction.

X-ray photoelectron spectra (XPS) were recorded using a hemispherical VG SCIENTA R3000 analyzer with constant pass energy of 100 eV, a monochromatized aluminum source Al Kα (E = 1486.6 eV) and a low energy electron flood gun (FS40A-PS) to compensate the charge on the surface of nonconductive samples. The base pressure in the analytical chamber was 5×10^{-9} mbar.

The binding energies were referenced to C 1s core level (E_b = 284.6 eV). The composition and chemical surrounding of the sample surface were investigated on the basis of the areas and binding energies of Ti 2p, O 1s, N 1s and C 1s photoelectron peaks. The fitting of high resolution spectra was provided through the Casa XPS software.

The morphology of particles was observed on a transmission electron microscope (TEM) JEOL 2010 HC (JEOL Ltd., Japan). The particles were dispersed in ethanol and using an ultrasonic sprayer deposited on a TEM grid with carbon holey support film.

Photoelectrochemical measurements were performed using a photoelectric spectrometer equipped with the 150 W Xe lamp and coupled with the P-IF 1.6 potentiostat (Instytut Fotonowy, Poland). The photocurrent responses were recorded using a classical three electrode setup. The platinum wire and Ag/AgCl were used as the auxiliary and reference electrodes, respectively. The working electrode consisted of photocatalyst powder deposited onto indium-tin oxide (ITO) foil coated by polyethylene terephthalate. The 0.1 M KNO_3 was used as an electrolyte solution. The photocurrent spectra were recorded within the range of 240 – 500 nm with the step of 10 nm in the potential range of - 0.2 to 0.8 V, step 0.1 V. Before the measurement itself the electrolyte was purged by argon to ensure oxygen free environment. The argon purge was also kept constant during the measurement.

2.3. Photocatalytic reduction of CO_2

The photocatalytic reduction of carbon dioxide was carried out in a homemade apparatus (

Figure 1). A cylindrical stirred batch reactor with a photocatalyst spread on the bottom of the reactor was illuminated by an 8 W Hg lamp (λ = 254 nm; intensity = 0.5 mW/cm^2) placed in horizontal position on top of the quartz glass visor. The reactor shell was made from stainless steel. The internal volume was 355 cm^3. The photocatalyst powder loading was 0.1 g. Before the

irradiation was turned ON, a supercritical fluid-grade CO_2 with a certified maximum of hydrocarbons less than 1 ppm (SIAD Technical Gases, CZ) to avoid any hydrocarbon contamination was purged through distilled water reservoir to saturate it by humidity (50 rel.%). Afterwards the water saturated CO_2 was purged through the reactor in order to displace the air from the reactor. The CO_2 pressure was maintained at 120 kPa through the purging for 20 minutes. The pressure inside the reactor was continuously monitored. The reactor was pressurized to 140 kPa and sealed. The sample at 0 hour was taken and immediately analyzed on barrier discharge ionization detector (GC/BID). The photocatalytic reaction was started by switching on the Hg lamp. Gas samples were discontinuously taken at various times during the irradiation (8 hours). Gas sampling was performed using a gas-tight syringe (10 ml) through a septum. GC/BID equipped by ShinCarbon ST micropacked column was used for the analysis of reaction products in the gas phase.

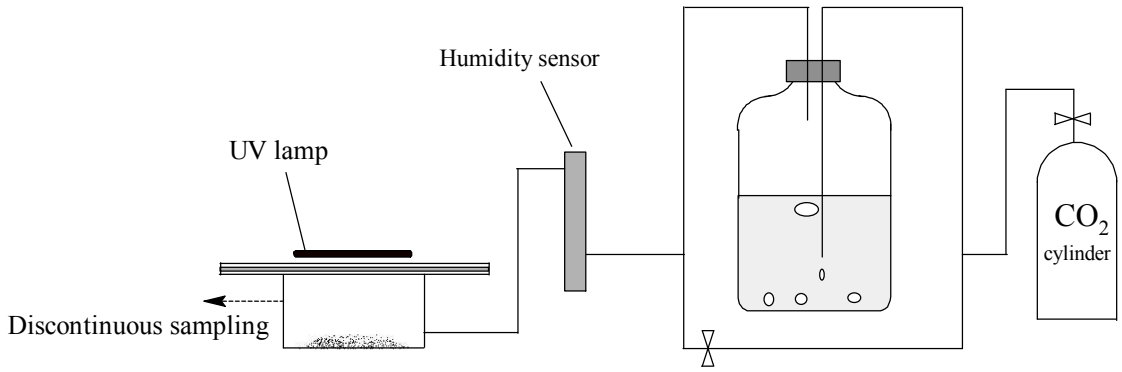

Figure 1: The schematic description of the CO_2 photocatalytic reduction apparatus.

The accuracy of the experiment was verified by a series of repeated measurements, and the relative error of product yields ($\mu mol/g_{cat}$) was determined to be less than 10 %. Blank tests were carried out to guarantee that the methane production was due to the photocatalytic reduction of CO_2 and to eliminate the surrounding interference. During the first test, the reactor was UV-

illuminated without the photocatalyst, the second blank test was conducted in the dark with the photocatalyst under the same experimental conditions, and the third test consisted of irradiating the photocatalyst in the absence of CO_2. No hydrocarbons were detected in the above blank tests.

To double check the products are really coming from the photocatalytic reduction of CO_2 the measurement with CO_2 containing ^{13}C isotope was conducted. Samples were taken at various times and the increase of ^{13}C amount in methane was observed with increasing irradiation time. These measurements confirmed that the methane is a product of the CO_2 photocatalytic reduction.

2.4. Photocatalytic reduction of N_2O

The photocatalytic reduction of N_2O was carried out in a homemade apparatus at ambient temperature with and without the photocatalyst (photocatalysis and photolysis, respectively) [12]. The 0.1 g of photocatalyst was placed on an adhesive tape inserted on the bottom of the batch reactor (635 ml volume). In both photochemical and photocatalytic experiments, the reactor was filled with a N_2O/He mixture (968 ppm) and irradiated by an 8 W Hg lamp (λ = 254 nm; intensity = 0.5 mW/cm^2). Pressure was continuously monitored inside the photoreactor during the experiments. A gas chromatograph equipped by ShinCarbon ST micropacked column and GC/BID was used for the analysis of N_2O decrease. The concentration of N_2O was measured before switching on the UV lamp to determine initial concentration and during the reaction. The reproducibility of the photocatalytic experiments was verified by repeated tests in the interval of 0–18 h. The accuracy of the measurement was certified by a series of repeated measurements, and the relative error of the N_2O concentration was determined to be less than 5 %.

3. Results and discussion

3.1. Photocatalysts characterization

Results from nitrogen physisorption, UV-Vis DRS and XRD are summarized in Tab. 1. The specific surface area of mixed photocatalysts increased significantly compared to pure g-C_3N_4. Due to very organized arrangement of g-C_3N_4 crystal lattice its specific surface area is very low. Usually the value is somewhere around 10 m^2/g [21, 39]. Excluding pure g-C_3N_4 all the prepared photocatalysts and TiO_2 Evonik P25 had very similar specific surface area with a value close to 50 m^2/g.

Absorption edge energy is one of the key aspects of the photocatalysis (Tab. 1). Graphitic C_3N_4 has relatively low band gap energy which is one of the reasons why this material attracted great attention of the photocatalytic society. The band gap energy of commercial TiO_2 Evonik P25 is quite high, 3.26 eV in our case and the addition of g-C_3N_4 decreased the absorption edge energy only slightly (Table 1). The absorption edge energies of photocatalysts were determined from UV-Vis DRS spectra (Figure 2b). Based on the UV-vis DRS spectra the blue shift can be observed after addition of TiO_2 to pure g-C_3N_4 (Figure 2a). The absorption edges of all TiO_2/g-C_3N_4 composites are the same within the experimental error. Therefore, the UV-vis DRS spectra of all composites are the same but different from pure TiO_2 and g-C_3N_4.

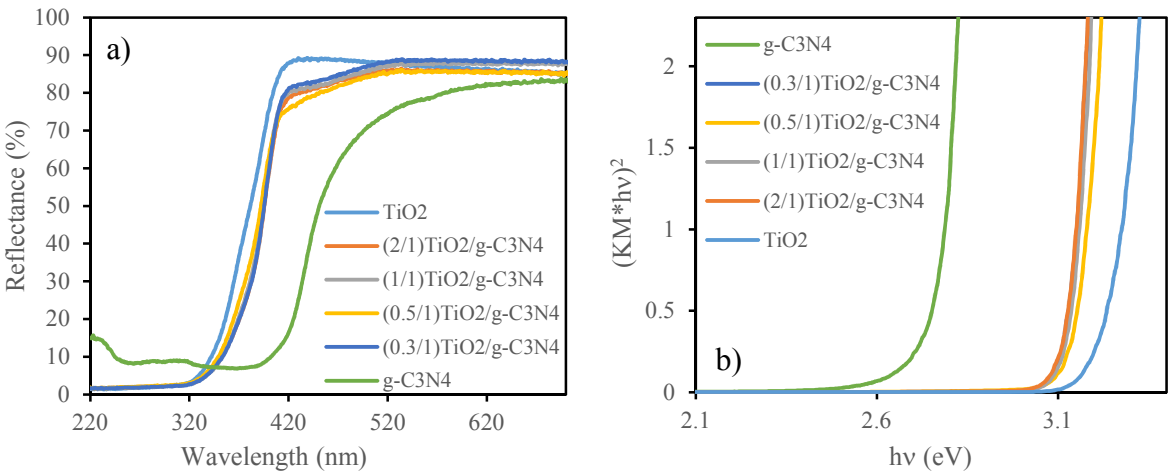

Figure 2: a) UV-Vis DRS spectra of TiO_2/g-C_3N_4 photocatalysts and b) the determination of the absorption edges of TiO_2/g-C_3N_4 photocatalysts.

Table 1: Specific surface area, absorption edge energy and crystallite size of prepared photocatalysts.

Photocatalyst	Specific surface area (m^2/g)	Absorption edge energy (eV)	Crystallite size (nm)	
			Anatase	Rutile
TiO_2 (Evonik P25)	51	3.26	20	29
(2/1)TiO_2/g-C_3N_4	43	3.13	23	42
(1/1)TiO_2/g-C_3N_4	48	3.16	24	41
(0.5/1)TiO_2/g-C_3N_4	49	3.16	23	43
(0.3/1)TiO_2/g-C_3N_4	53	3.13	23	28
g-C_3N_4	11	2.78	-----	-----

The commercial TiO_2 is composed from anatase and rutile phase which was confirmed by Raman spectroscopy (Figure 3a). The Ti–O vibrational modes of anatase are located around 395, 515 and 640 cm^{-1}. The Ti–Ti vibrational modes of anatase are located at 140 and 195 cm^{-1} [40, 41]. Rutile's Ti–O vibrational modes are located around 445, 610, 825 cm^{-1} and Ti–Ti vibrational mode of rutile is located around 140 cm^{-1} [41]. Since the rutile phase is representing the minority, the only recognizable peaks were at 445 and 791 cm^{-1}. The other ones are being overlapped by the anatase vibrational modes.

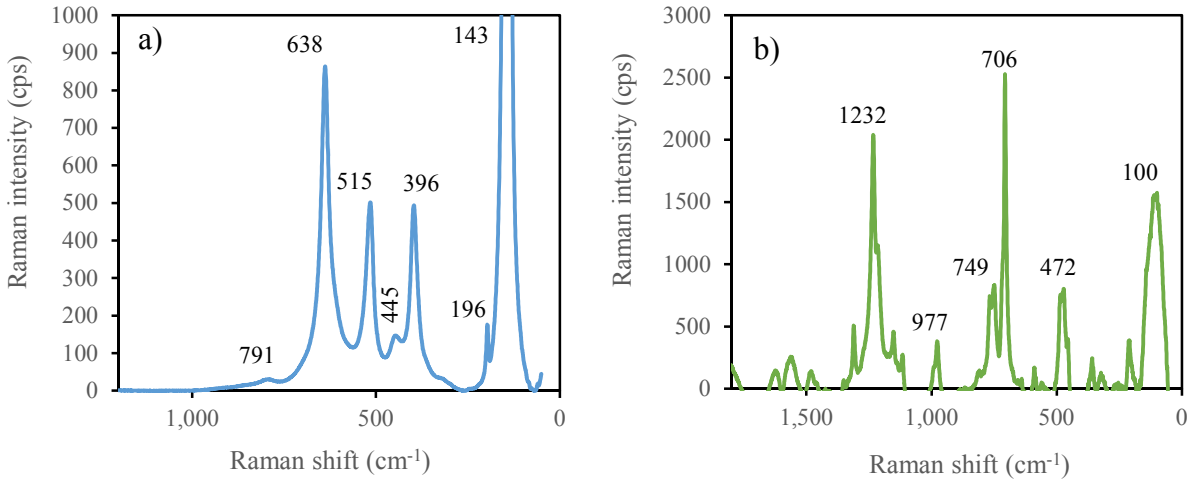

Figure 3: Raman spectra of a) commercial TiO_2 Evonik P25 and b) g-C_3N_4.

The interpretation of pure g-C_3N_4 Raman spectra is a little bit more complicated (Figure 3b). The number of vibrational modes and their intensity depends on calcination temperature and temperature ramp rate. Characteristic peaks for g-C_3N_4 calcined at 550°C can be found at 472, 712, 751, 980, 1152 and 1226 cm^{-1} [42, 43].

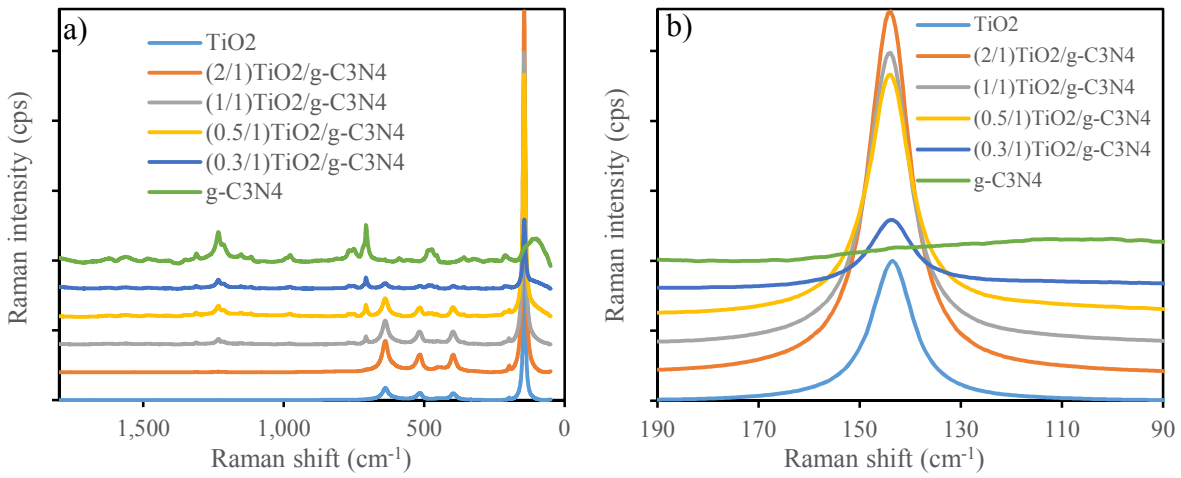

Figure 4: a) Raman spectra of all prepared photocatalysts; b) evolution of the Raman spectra focused on TiO_2 characteristic peak at 143 cm^{-1}.

Figure 4a shows the Raman spectra of all investigated photocatalysts. The decrease of TiO_2 characteristic peaks intensity and increase of g-C_3N_4 peaks intensity can be observed with decreasing ratio of TiO_2/g-C_3N_4. Also no peak shifts were observed which means no structural changes occurred during preparation of mixed photocatalysts regarding to pure TiO_2 and g-C_3N_4. For better resolution the most intense anatase peak part is shown in Figure 4b.

The FT-IR spectra of prepared g-C_3N_4, TiO_2 Evonik P25 and TiO_2/g-C_3N_4 photocatalysts are shown in Figure 5. In the FT-IR spectra of g-C_3N_4 the strong band region from 1200 to 1650 cm^{-1} can be found. The peak at 1640 cm^{-1} is attributed to C–N stretching, while three bands at 1555, 1461 and 1405 cm^{-1} are the result of the typical stretching vibrations of C–N heterocycles [44, 45]. The last two bands at 1319 and 1243 cm^{-1} of the region belong to stretching vibration of connected units of C–NH–C, which is also supported by the broad band at 2900 – 3500 cm^{-1}. This broad band is attributed to N–H and O–H stretches due to the free amino groups and adsorbed hydroxyl species, respectively [45]. The peak at 806 cm^{-1} is attributed to the characteristic breathing mode of s-triazine [44, 45], which increases with the increase of the g-C_3N_4 content. All

the g-C_3N_4 characteristic bands are also present in the mixtures of TiO_2/g-C_3N_4 with decreasing intensity as the ratio of TiO_2/g-C_3N_4 increase. The following bands are typical for TiO_2 based materials. The broad band in the region of 3200 – 3600 cm^{-1} can be assigned to OH stretching modes. The two very small hard recognizable bands at 1600 and 1400 cm^{-1} are attributed to bending OH modes of hydroxyl groups. The broad band below at 900 cm^{-1} belongs to Ti–O vibrations [46].

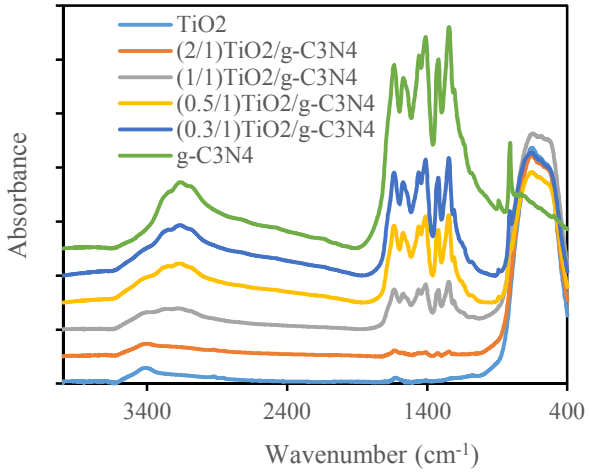

Figure 5: FT-IR spectra of TiO_2/g-C_3N_4 photocatalysts.

The photoluminescence spectra of the TiO_2/g-C_3N_4 samples are shown on Figure 6. All samples exhibit similar profiles with a broad emission band from 435 to 600 nm under an excitation wavelength of 325 nm. These spectra imply that PL intensities of the prepared nanocomposites are strongly dependent on recombination of charge carriers mainly in g-C_3N_4. The pure g-C_3N_4 has strong PL emission at wavelength between 440 - 500 nm which is caused by fast radiative recombination of electron and holes in the planar structure of g-C_3N_4. Position of emission band of g-C_3N_4 depends strongly on preparation conditions [47]. Weaker PL emission intensity is caused by electrons and holes transfer between g-C_3N_4 and TiO_2 [48, 49]. With increasing content of TiO_2 the probability of recombination between electrons and holes in

prepared samples significantly dropped. Similar results was observed on the g-C_3N_4-TiO_2 heterojunction systems by other groups [28, 50, 51].

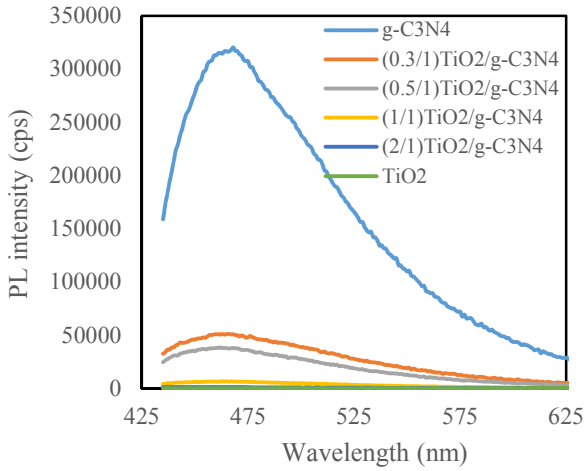

Figure 6: Photoluminescence spectra of TiO_2/g-C_3N_4 photocatalysts.

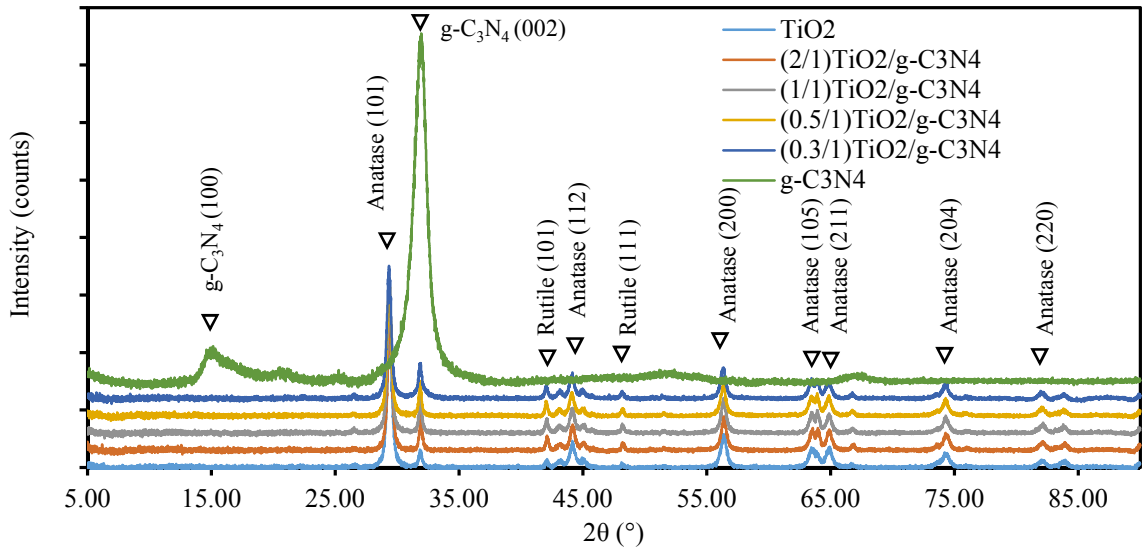

Figure 7: XRD patterns of TiO_2/g-C_3N_4 photocatalysts.

Two main diffraction peaks for g-C_3N_4 located at around 14.89 and 31.95°, were observed and indexed as (100) and (002) planes, respectively (Figure 7). These two diffraction peaks are in good agreement with the g-C_3N_4 (JCPDS no. 87–1526) [50]. Titanium dioxide was identified in composite samples in anatase (JCPDS no. 084–1285) and rutile (JCPDS no. 079–6029) forms. The crystallite size of the TiO_2 was determined from the half-width of peaks using Scherrer's formula (where K=0.89) on the anatase (101) and rutile (110) peaks. The intensity of g-C_3N_4 peaks in TiO_2 composites was attenuated in a simile way as reported [52]. The presence of g-C_3N_4 did not have a significant influence on the phase structure of TiO_2.

In Figure 8 the examples of high-resolution XPS spectra of elements identified on the surface of TiO_2/g-C_3N_4 photocatalyst with the highest g-C_3N_4 loading are shown in comparison to those measured for pure TiO_2 and g-C_3N_4. The C 1s spectrum of (0.3/1)TiO_2/g-C_3N_4 can be deconvoluted into two peaks at 284.6 eV (C1) and 288.1 eV (C2) attributed to C-C (contaminated carbon) and N=C-N (sp^2-bonded carbon in carbon nitride) coordination, respectively [53, 54]. Moreover, three components are identified in the XPS N 1s spectrum of this sample at 398.5 eV (N1), 399.8 eV (N2) and 401.1 eV (N3), corresponding to the N atoms in the C=N-C groups, the sp^2 hybridized N atoms and the sp^3 hybridized terminal N atoms in the heptazine rings (-NH_2), respectively [53, 54]. A slight shift (0.2-0.3 eV) towards lower binding energies for the C2, N1 and N2 peaks related to the N=C-N species is detected after the addition of TiO_2 to g-C_3N_4. This finding indicates changes in electron cloud density in the nitrogen and carbon atoms, which can result from the interaction of carbon nitride with titania. On the other hand, the Ti 2p spectra of commercial titania before and after doping with g-C_3N_4 show only two photoelectron peaks at 458.2-458.3 eV and 464.0-464.1 eV, with a peak separation of 5.7-5.8 eV, which correspond to Ti^{4+} $2_{p3/2}$ and Ti^{4+} $2_{p1/2}$, respectively [55]. The detectable changes in the peak

positions are observed in the high-resolution XPS O 1s spectra for pure TiO_2 and TiO_2 mixed with g-C_3N_4. Among two main O 1s components found in pure TiO_2, attributed to lattice O^{2-} (529.5 eV) and the O^{2-} ions/hydroxyl groups (530.6 eV) [56], the latter one is shifted to 530.9 eV in the case of (0.3/1)TiO_2/g-C_3N_4, confirming the occurrence of interactions between TiO_2 and g-C_3N_4 in the formed composites.

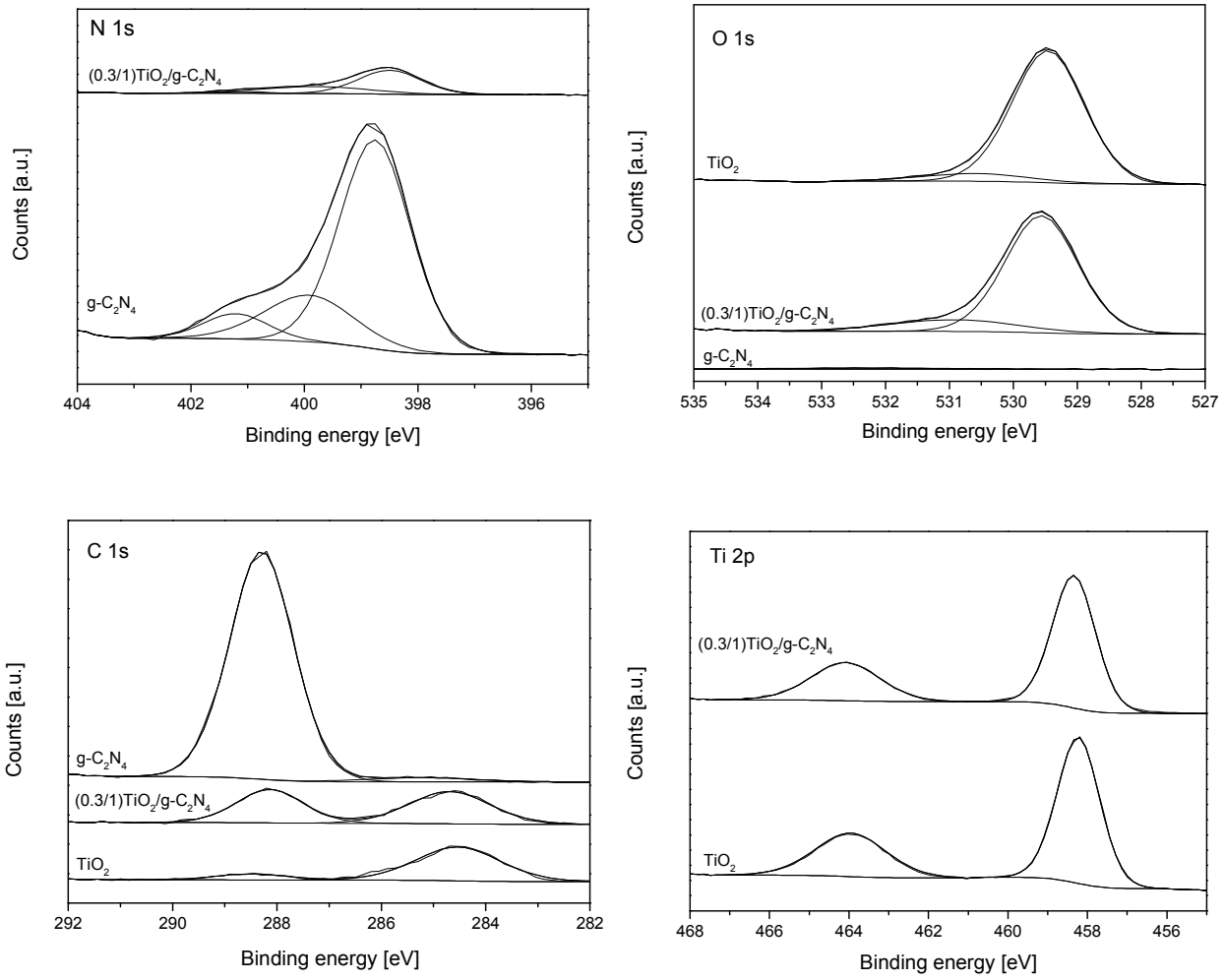

Figure 8: XPS N 1s, O 1s, C 1s and Ti 2p spectra measured for TiO_2, (0.3/1)TiO_2/g-C_3N_4 and g-C_3N_4.

The morphology of the photocatalysts was examined by TEM. Figure 9 shows the TEM images of g-C_3N_4, TiO_2, and (0.3/1)TiO_2/g-C_3N_4. It can be seen that pure g-C_3N_4 (Figure 9a) indicates a 2D lamellar structure while pure TiO_2 (Figure 9b) shows spherical particles. For (0.3/1)TiO_2/g-C_3N_4 (Figure 9c,d), the TiO_2 particles are embedded in the g-C_3N_4 lamellar structure. This finding suggests the creation of a heterojunction between TiO_2 and g-C_3N_4, which could lead to improved separation of electron and hole.

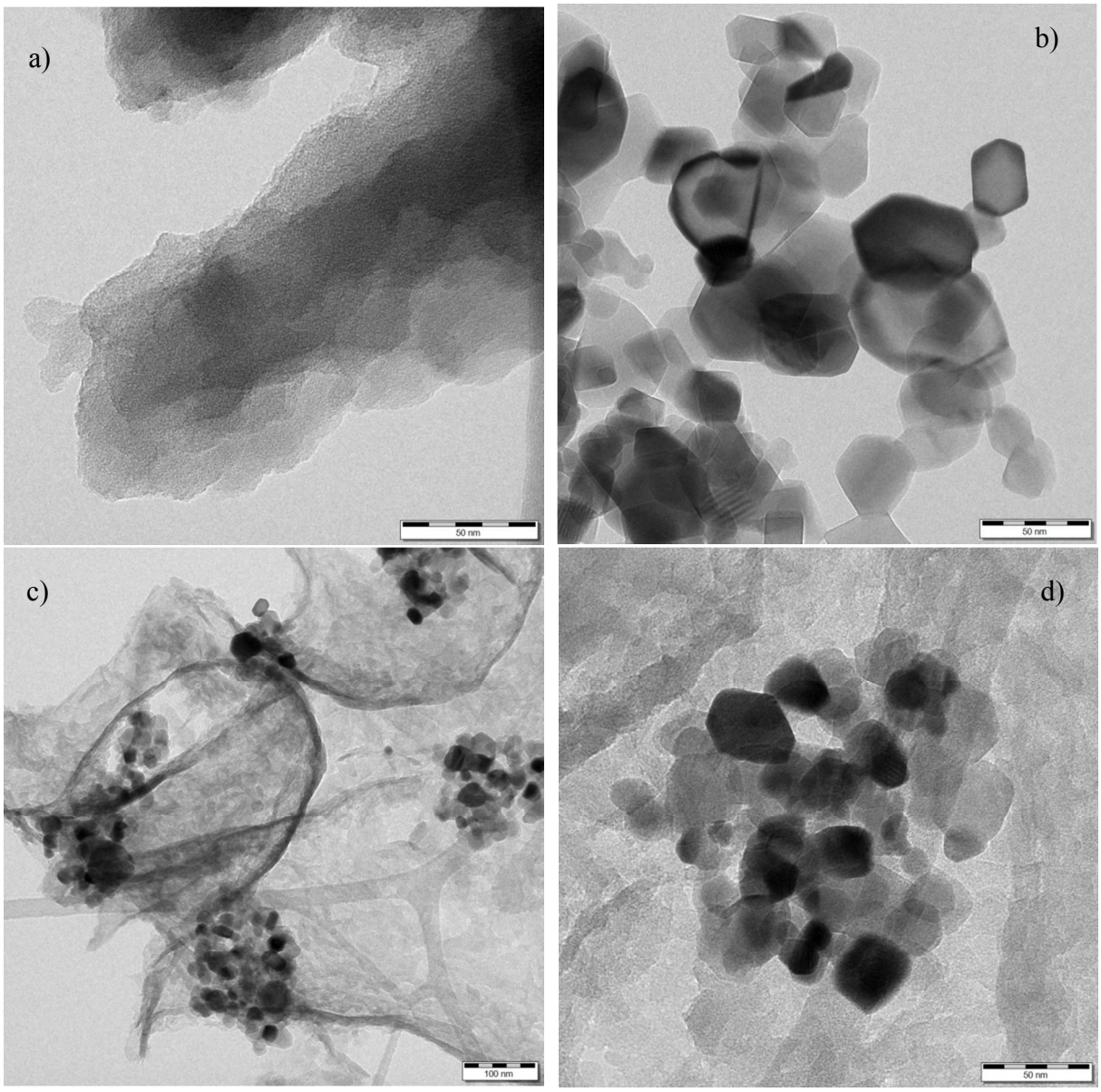

Figure 9: TEM images of g-C_3N_4(a), TiO_2 (b), and (0.3/1)TiO_2/g-C_3N_4 (c, d).

The photocurrent measurements were conducted to predict the photocatalytic activity of the prepared photocatalysts (Figure 10). It is evident all the prepared photocatalysts except pure g-C_3N_4 show large increase of generated photocurrent after switching the light source ON. The results revealed the pure g-C_3N_4 has the highest rate of charge carriers' recombination which in agreement with experimental data. On the other hand, the measurements suggest the (0.3/1)TiO_2/g-C_3N_4 and pure TiO_2 possess the most efficient separation of electrons and holes.

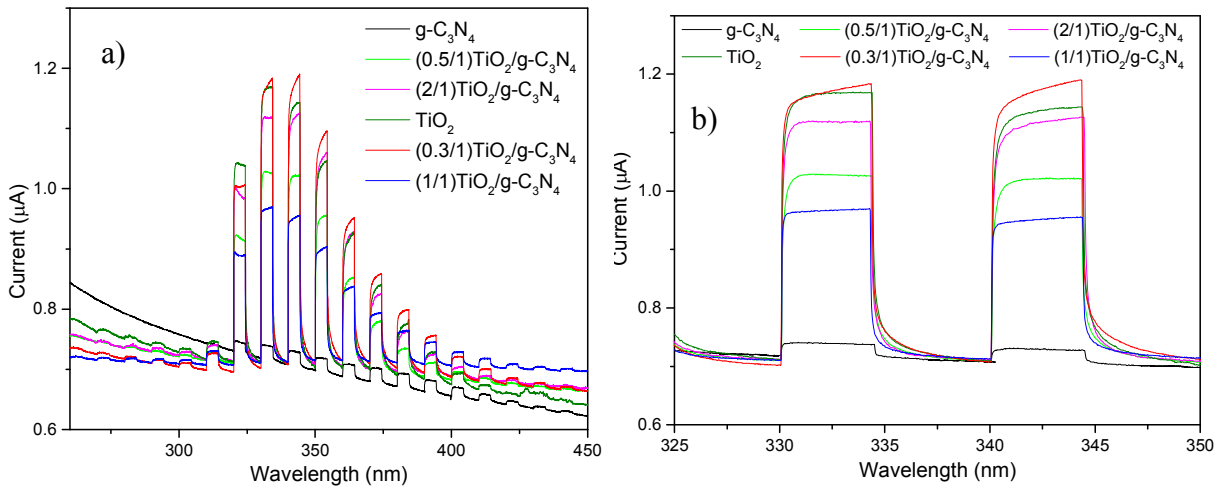

Figure 10: a) Photocurrent generation at electrodes made from the studied photocatalysts and b) cutoff interval of wavelengths recorded at 0.8 V *vs.* Ag/AgCl in deoxygenated 0.1 M KNO_3.

3.2. Photocatalytic reduction of CO_2

The effect of irradiation time on the formation of gaseous products in the photocatalytic reduction of carbon dioxide was studied in the presence of all prepared TiO_2/g-C_3N_4 photocatalysts including pure TiO_2 Evonik P25 and g-C_3N_4. Figure 11 demonstrates the evolution of CO_2 photocatalytic reduction products as the function of irradiation time. Methane and carbon monoxide are the direct products of CO_2 reduction. The methane production rate is more or less linear in the first 8 hours of irradiation (Figure 11a); carbon monoxide yields on the

other hand, rapidly increase in first 2 hours and then are almost constant (Figure 11b). The last detected product was hydrogen which is coming from the photocatalytic water (vapor) splitting (Figure 11c). The highest yields of the three products were reached in the presence of (0.3/1)TiO_2/g-C_3N_4. On the other hand, the lowest products production was achieved over pure g-C_3N_4.

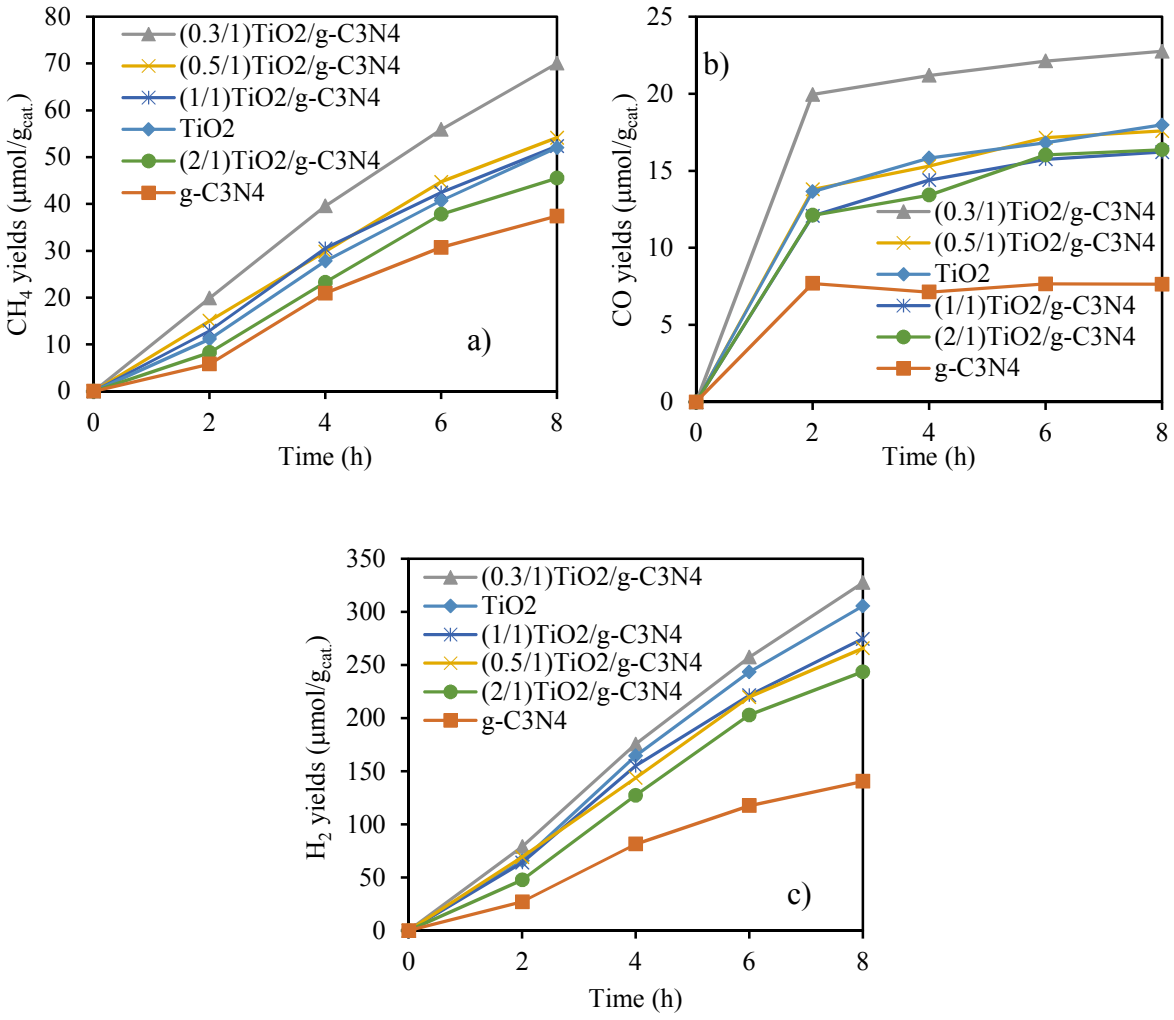

Figure 11: Time dependence of the a) methane yields, b) carbon monoxide yields and c) hydrogen yields over TiO_2/g-C_3N_4 photocatalysts in the CO_2 photocatalytic reduction.

Conditions: 8 W Hg lamp, CO_2 pressure at carbonation of 120 kPa, humidity 50%, photocatalyst loading of 0.1 g.

3.3. Photocatalytic reduction of N_2O

The effect of irradiation time on the photochemical and photocatalytic decomposition of N_2O was investigated for all TiO_2/g-C_3N_4 photocatalysts including pure TiO_2 and g-C_3N_4 for a time period of 0–16 h. The time dependences of N_2O conversion for photocatalysis and photolysis are shown in Figure 12. A gradual increase of N_2O conversion with increasing time of irradiation can be noticed. The highest N_2O conversion of 57 % was observed for the (0.3/1)TiO_2/g-C_3N_4 catalyst after 16 h. On the other hand, both pure TiO_2 and g-C_3N_4 photocatalysts exhibited the same N_2O conversions as during the photolysis experiments. The products of the reaction are oxygen and nitrogen; no other compounds were detected.

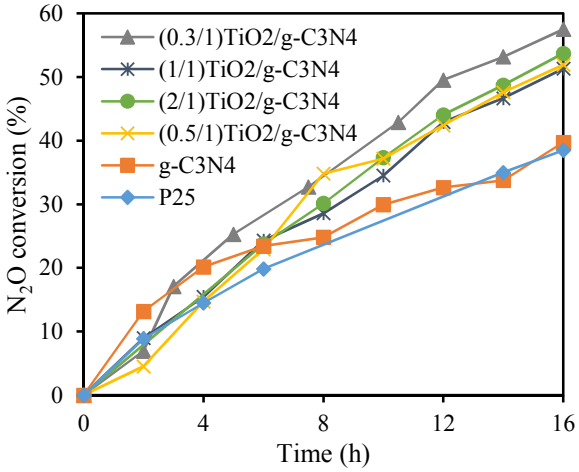

Figure 12: Time dependence of the N_2O conversion over TiO_2/g-C_3N_4 photocatalysts. Conditions: 8 W Hg lamp, N_2O (968 ppm)/He mixture, photocatalyst loading of 0.1 g.

3.4. Factors influencing the photocatalytic reduction of CO_2 and N_2O over different TiO_2/g-C_3N_4 photocatalysts

The most active photocatalyst in both cases, the photocatalytic reduction of CO_2 and N_2O, respectively, was the one composed of 0.3/1 ratio of TiO_2/g-C_3N_4. The photocatalytic experiments showed the ratio of TiO_2 and g-C_3N_4 plays significant role in photocatalysis. It also confirmed pure g-C_3N_4 is not very active photocatalyst due to its high recombination rate of charge carriers and very low specific surface area [15]. The very high recombination of g-C_3N_4 also confirms photoluminescence spectra where the g-C_3N_4 band has the intensity several times higher than the rest of the photocatalysts (Figure 6).

Even though both studied reactions are reductions the reaction mechanism is different for each of them. Photocatalytic reduction of carbon dioxide heavily depends on sufficient potentials of photocatalyst's conduction and valence bands. CO_2 molecule is very stable and direct reduction by electron ($CO_2/CO_2^{\bullet}$) is limited by very negative potential (–1.9 V vs. NHE) [6, 57]. The main products of the photocatalytic reduction of CO_2 are methane and carbon monoxide and also by-product hydrogen. Hydrogen is produced from water which is present in the form of vapor. The most important redox potentials vs. NHE are given in Eqs. (3) – (8) [6]:

$$2\ H^+ + 2\ e^- \rightarrow H_2 \qquad E^0 = -0.41\ V \qquad (3)$$

$$CO_2 + 2\ H^+ + 2\ e^- \rightarrow CO + H_2O \qquad E^0 = -0.53\ V \qquad (4)$$

$$CO_2 + 8\ H^+ + 8\ e^- \rightarrow CH_4 + 2\ H_2O \qquad E^0 = -0.24\ V \qquad (5)$$

$$2\ H_2O + 4\ h^+ \rightarrow O_2 + 4\ H^+; \qquad E^0 = +0.82\ V \qquad (6)$$

$$H_2O + h^+ \rightarrow OH^{\bullet} + H^+; \qquad E^0 = +2.32\ V \qquad (7)$$

$$O_2 + e^- \rightarrow O_2^{\bullet -}; \qquad E^0 = -0.33\ V \qquad (8)$$

The pure g-C_3N_4 proved to be the least efficient towards any of the products. This is in agreement with g-C_3N_4 valence band not having sufficient potential of generated holes for oxidation of water to hydroxyl radicals (5). Only the less effective water oxidation, due to more

holes needed to achieve it, can be conducted. Because of this limitation, lower amounts of H^+ are formed and through these lower yields of all products were detected. The pure TiO_2 on the other hand gives the average yields of CH_4 and CO and the higher yields of H_2.

In case of the nitrous oxide reduction the potential of N_2O/N_2 redox couple is around 1.35 V which fits in between of valence and conduction bands of both, TiO_2 and g-C_3N_4 as well. Nevertheless, pure TiO_2 and C_3N_4, respectively showed no photocatalytic activity, the results were the same as in case of photolysis. The addition of TiO_2 to C_3N_4 improved the conversion about over 10 %.

The photocatalytic activity of semiconductor nanomaterials can be influenced by several aspects such as: (i) specific surface area, (ii) adsorption edge energy, (iii) crystallite size and (iv) efficient separation of the charge carriers. All these factors can be significantly influenced by the formation of TiO_2/g-C_3N_4 nanomaterials, which are formed by the addition of g-C_3N_4 to the TiO_2.

For (i), specific surface area of TiO_2/g-C_3N_4 has increased with increasing amount of g-C_3N_4. The increase of the BET specific surface area of TiO_2/g-C_3N_4 could be explained due to TiO_2 nanoparticles embedded in the g-C_3N_4 lamellar structure leads to the formation of thinner lamellar g-C_3N_4 (Figure 9). The grinding may lead to the exfoliation of g-C_3N_4, which increases the surface areas of the photocatalysts. The similar results were obtained by [50]. The higher specific surface area can offer more available active sites and due to that higher photoactivity. The (0.3/1)TiO_2/g-C_3N_4 has shown the highest specific surface area (S_{BET} = 53 m^2/g) in comparison with pure g-C_3N_4 (S_{BET} = 11 m^2/g) and also the highest photoactivity. On the other hand, the decrease of specific surface area with increase of TiO_2 content can be explained by agglomerating of TiO_2 (Figure 9c, d).

For (ii), all the prepared TiO_2/g-C_3N_4 demonstrated lower absorption edge energy (Table 1) and simultaneously suitable position of conduction and valence bands in comparison with pure TiO_2. The decrease of the absorption edge energy is leading to increased effectivity of electron hole pair generation due to the absorption of lower energy photons.

For (iii), crystallinity size of rutile can also influence the photocatalytic activity due to formation of defects. Formation of lattice defects is enhancing electron-hole recombination resulting in lower photocatalytic activity [58]. The (0.3/1)TiO_2/g-C_3N_4 proved to have the smallest crystallite size of rutile from all the composites and this fact probably also contributed to the higher photoactivity of this photocatalyst.

For (iv), the efficient separation of the charge carriers plays probably key role in photocatalytic activity of TiO_2/g-C_3N_4 nanocomposites. The electronic structure of the photocatalyst determines whether the material is going to be active towards specific reaction or not. The conduction band potentials of g-C_3N_4 and TiO_2 are –1.15 V and –0.3 V, respectively. The valence bands of g-C_3N_4 and TiO_2 have potentials at 1.5 V and 3.0 V, respectively. The quite big difference between electronic bands potentials of g-C_3N_4 and TiO_2 makes the combination of these two materials very interesting. The electrons that are photogenerated from the semiconductor with a higher CB edge (the g-C_3N_4) migrate to the one with a lower CB edge (TiO_2). Furthermore, the photogenerated holes are transported from the low VB of TiO_2 to the high VB of g-C_3N_4 between the semiconductors [59]. This leads to the accumulation of electrons on TiO_2 semiconductor for a reduction reaction and accumulation of holes in g-C_3N_4 semiconductor for an oxidation reaction (Figure 13). Therefore, the electrons and holes are spatially separated to effectively repress charge recombination [59].

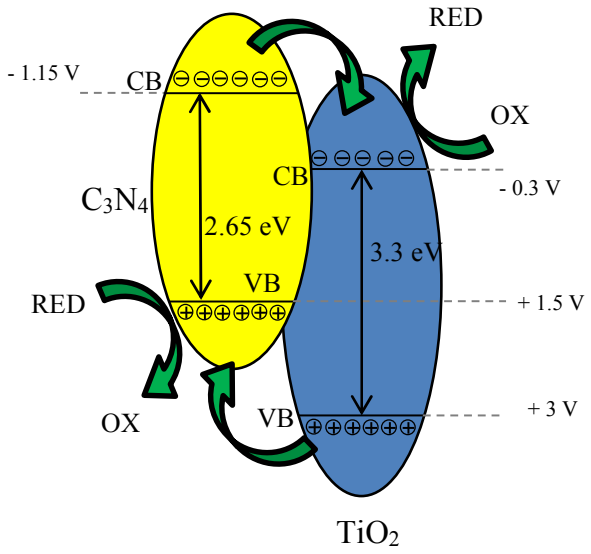

Figure 13: Schematic illustration showing the photogenerated charge separation in TiO_2/g-C_3N_4 photocatalysts.

The enhancement in photocatalytic performance can be attributed to the synergetic effect of the surface area, crystallite size of rutile, absorption edge energy and mainly separation of the charge carriers which is confirmed by a higher activity of the prepared TiO_2/g-C_3N_4 nanocomposites compared to pure g-C_3N_4. The optimal ratio of TiO_2 to C_3N_4 have been found to be 0.3 to 1. The similar result was observed by Li et. al. who found, that the most active g-C_3N_4/TiO_2 composite sample investigated for methyl orange degradation contained 74.4 wt.% of g-C_3N_4 [60].

4. Conclusion

A series of TiO_2/g-C_3N_4 photocatalysts with different ratio of TiO_2 to g-C_3N_4 (from 0.3/1 to 2/1) have been fabricated by mechanical mixing of g-C_3N_4 prepared from melamine and

commercial TiO_2 Evonik P25. The photocatalytic activity results from photocatalytic CO_2 reduction and NO_2 decomposition revealed that all of the synthesized TiO_2/g-C_3N_4 photocatalysts had enhanced photocatalytic performance compared to their components especially to g-C_3N_4. The highest photocatalytic activity of these photocatalysts can be explained by the combination of several aspects: (i) specific surface area, (ii) adsorption edge energy, (iii) crystallite size and (iv) efficient separation of the charge carriers. The most active photocatalyst towards both oxides reduction was (0.3/1)TiO_2/g-C_3N_4. Based on the obtained results it can be assumed that the semiconductor nanocomposite formed between g-C_3N_4 and TiO_2 can have application for photocatalytic reaction in environmental remediation.

Corresponding Author

*Martin Reli, Institute of Environmental Technology, VŠB-TU Ostrava, 17. listopadu 15/2172, 708 33 Ostrava, Czech Republic, e-mail: martin.reli@vsb.cz; tel.: +420 597 327 304

Acknowledgements

This work was supported by the Grant Agency of the Czech Republic (projects. reg. No. 14-35327J and 16-10527S), by the Ministry of Education, Youth and Sports of the Czech Republic within "National Feasibility Program I", project LO1404 "TUCENET" and by EU structural funding Operational Programme Research and Development for Innovation Project No. CZ.1.05/2.1.00/19.0388.

References

1. de Richter, R.; Caillol, S. Fighting global warming: The potential of photocatalysis against CO_2, CH_4, N_2O, CFCs, tropospheric O_3, BC and other major contributors to climate change. *J. Photoch. photobio. C* **2011,** *12*, 1-19.
2. de Richter, R. K.; Ming, T.; Caillol, S. Fighting global warming by photocatalytic reduction of CO_2 using giant photocatalytic reactors. *Renew. Sust. Energ. Rev.* **2013,** *19*, 82-106.

3. Olivier, J.; Janssens-Maenhout, G. *CO_2 emissions from fuel combustion highlights*. International Energy Agency: France, 2014; p 136.
4. NOAA CO_2 now. http://co2now.org/ (accessed 12/12/2015).
5. Inoue, T.; Fujishima, A.; Konishi, S.; Honda, K. Photoelectrocatalytic reduction of carbon-dioxide in aqueous suspensions of semiconductor powders. *Nature* **1979,** *277*, 637-638.
6. Habisreutinger, S. N.; Schmidt-Mende, L.; Stolarczyk, J. K. Photocatalytic reduction of CO_2 on TiO_2 and other semiconductors. *Angew. Chem. Int. Ed. Engl.* **2013,** *52*, 7372-7408.
7. Li, K.; An, X.; Park, K. H.; Khraisheh, M.; Tang, J. A critical review of CO_2 photoconversion: Catalysts and reactors. *Catal. Today* **2014,** *224*, 3-12.
8. Liu, L. Understanding the reaction mechanism of photocatalytic reduction of CO_2 with H_2O on TiO_2-based photocatalysts: A review. *Aerosol Air Qual. Res.* **2014**, 453-469.
9. Yuan, L.; Xu, Y.-J. Photocatalytic conversion of CO_2 into value-added and renewable fuels. *Appl. Surf. Sci.* **2015,** *342*, 154-167.
10. Ju, W. S.; Matsuoka, M.; Anpo, M. The photocatalytic reduction of nitrous oxide with propane on lead(II) ion-exchanged ZSM-5 catalysts. *Catal. Lett.* **2001,** *71*, 91-93.
11. Matsuoka, M.; Ju, W.-S.; Yamashita, H.; Anpo, M. In situ characterization of the Ag^+ ion-exchanged zeolites and their photocatalytic activity for the decomposition of N_2O into N_2 and O_2 at 298 K. *J. Photochem. Photobiol. A* **2003,** *160*, 43-46.
12. Matějová, L.; Šihor, M.; Brunátová, T.; Ambrožová, N.; Reli, M.; Čapek, L.; Obalová, L.; Kočí, K. Microstructure-performance study of cerium-doped TiO_2 prepared by using pressurized fluids in photocatalytic mitigation of N_2O. *Res. Chem. Intermed.* **2015**, 1-15.
13. Obalová, L.; Reli, M.; Lang, J.; Matějka, V.; Kukutschová, J.; Lacný, Z.; Kočí, K. Photocatalytic decomposition of nitrous oxide using TiO_2 and Ag-TiO_2 nanocomposite thin films. *Catal. Today* **2013,** *209*, 170-175.
14. Obalová, L.; Šihor, M.; Praus, P.; Reli, M.; Kočí, K. Photocatalytic and photochemical decomposition of N_2O on ZnS-MMT catalyst. *Catal. Today* **2014,** *230*, 61-66.
15. Dong, G.; Zhang, Y.; Pan, Q.; Qiu, J. A fantastic graphitic carbon nitride (g-C_3N_4) material: Electronic structure, photocatalytic and photoelectronic properties. *J. Photochem. Photobiol. C* **2014,** *20*, 33-50.
16. Ye, S.; Wang, R.; Wu, M.-Z.; Yuan, Y.-P. A review on g-C_3N_4 for photocatalytic water splitting and CO_2 reduction. *Appl. Surf. Sci.* **2015,** *358, Part A*, 15-27.
17. Liu, C.; Huang, H.; Du, X.; Zhang, T.; Tian, N.; Guo, Y.; Zhang, Y. In situ co-crystallization for fabrication of g-C_3N_4/Bi_5O_7I heterojunction for enhanced visible-light photocatalysis. *J. Phys. Chem. C* **2015,** *119*, 17156-17165.
18. Tian, N.; Huang, H.; He, Y.; Guo, Y.; Zhang, T.; Zhang, Y. Mediator-free direct Z-scheme photocatalytic system: $BiVO_4$/g-C_3N_4 organic-inorganic hybrid photocatalyst with highly efficient visible-light-induced photocatalytic activity. *Dalton Trans.* **2015,** *44*, 4297-4307.
19. Tian, N.; Huang, H.; Liu, C.; Dong, F.; Zhang, T.; Du, X.; Yu, S.; Zhang, Y. In situ co-pyrolysis fabrication of CeO_2/g-C_3N_4 n-n type heterojunction for synchronously promoting photo-induced oxidation and reduction properties. *J. Mater. Chem. A* **2015,** *3*, 17120-17129.
20. Yu, W.; Xu, D.; Peng, T. Enhanced photocatalytic activity of g-C_3N_4 for selective CO_2 reduction to CH_3OH via facile coupling of ZnO: a direct Z-scheme mechanism. *J. Mater. Chem. A* **2015,** *3*, 19936-19947.
21. Boonprakob, N.; Wetchakun, N.; Phanichphant, S.; Waxler, D.; Sherrell, P.; Nattestad, A.; Chen, J.; Inceesungvorn, B. Enhanced visible-light photocatalytic activity of g-C_3N_4/TiO_2 films. *J. Colloid Interface Sci.* **2014,** *417*, 402-409.

22. Gu, L.; Wang, J.; Zou, Z.; Han, X. Graphitic-C_3N_4-hybridized TiO_2 nanosheets with reactive {0 0 1} facets to enhance the UV- and visible-light photocatalytic activity. *J. Hazard. Mater.* **2014,** *268*, 216-223.
23. Lei, J.; Chen, Y.; Shen, F.; Wang, L.; Liu, Y.; Zhang, J. Surface modification of TiO_2 with g-C_3N_4 for enhanced UV and visible photocatalytic activity. *J. Alloys Compd.* **2015,** *631*, 328-334.
24. Lu, D.; Zhang, G.; Wan, Z. Visible-light-driven g-C_3N_4/Ti^{3+}-TiO_2 photocatalyst co-exposed {0 0 1} and {1 0 1} facets and its enhanced photocatalytic activities for organic pollutant degradation and Cr(VI) reduction. *Appl. Surf. Sci.* **2015,** *358, Part A*, 223-230.
25. Song, G.; Chu, Z.; Jin, W.; Sun, H. Enhanced performance of g-C_3N_4/TiO_2 photocatalysts for degradation of organic pollutants under visible light. *Chin. J. Chem. Eng.* **2015,** *23*, 1326-1334.
26. Hao, R.; Wang, G.; Tang, H.; Sun, L.; Xu, C.; Han, D. Template-free preparation of macro/mesoporous g-C_3N_4/TiO_2 heterojunction photocatalysts with enhanced visible light photocatalytic activity. *Appl. Catal. B* **2016,** *187*, 47-58.
27. Chen, L.; Zhou, X.; Jin, B.; Luo, J.; Xu, X.; Zhang, L.; Hong, Y. Heterojunctions in g-C_3N_4/B-TiO_2 nanosheets with exposed {001} plane and enhanced visible-light photocatalytic activities. *Int. J. Hydrogen Energy* **2016,** *41*, 7292-7300.
28. Mohini, R.; Lakshminarasimhan, N. Coupled semiconductor nanocomposite g-C_3N_4/TiO_2 with enhanced visible light photocatalytic activity. *Mater. Res. Bull.* **2016,** *76*, 370-375.
29. Chang, F.; Zhang, J.; Xie, Y.; Chen, J.; Li, C.; Wang, J.; Luo, J.; Deng, B.; Hu, X. Fabrication, characterization, and photocatalytic performance of exfoliated g-C_3N_4–TiO_2 hybrids. *Appl. Surf. Sci.* **2014,** *311*, 574-581.
30. Li, J.; Zhang, M.; Li, Q.; Yang, J. Enhanced visible light activity on direct contact Z-scheme g-C_3N_4-TiO_2 photocatalyst. *Appl. Surf. Sci.* **2016**, in press.
31. Li, Y.; Wang, R.; Li, H.; Wei, X.; Feng, J.; Liu, K.; Dang, Y.; Zhou, A. Efficient and stable photoelectrochemical seawater splitting with TiO_2@g-C_3N_4 nanorod arrays decorated by Co-Pi. *J. Phys. Chem. C* **2015,** *119*, 20283-20292.
32. Yu, J.; Wang, S.; Low, J.; Xiao, W. Enhanced photocatalytic performance of direct Z-scheme g-C_3N_4-TiO_2 photocatalysts for the decomposition of formaldehyde in air. *Phys. Chem. Chem. Phys.* **2013,** *15*, 16883-16890.
33. Zhou, D.; Chen, Z.; Yang, Q.; Dong, X.; Zhang, J.; Qin, L. In-situ construction of all-solid-state Z-scheme g-C_3N_4/TiO_2 nanotube arrays photocatalyst with enhanced visible-light-induced properties. *Sol. Energy Mater. Sol. Cells* **2016,** *157*, 399-405.
34. Gregg, S. J.; Sing, K. S. W. *Adsorption. Surface Area and Porosity*. Academic: New York, 1982.
35. Schneider, P. Adsorption isotherms of microporous-mesoporous solids revisited. *Appl. Catal. A* **1995,** *129*, 157-165.
36. Deboer, J. H.; Lippens, B. C.; Linsen, B. G.; Broekhof.Jc; Vandenhe.A; Osinga, T. J. T-curve of multimolecular N_2-adsorption. *J. Colloid Interface Sci.* **1966,** *21*, 405-414.
37. Lecloux, A.; Pirard, J. P. The importance of standard isotherms in the analysis of adsorption isotherms for determining the porous texture of solids. *J. Colloid Interface Sci.* **1979,** *70*, 265-281.
38. Barret, E. P.; Joyner, L. G.; Halenda, P. B. The determination of the pore volume and area distributions in porous substances. I. Computations from nitrogen isotherms. *J. Am. Chem. Soc.* **1951,** *73*, 373-380.

39. Dai, K.; Lu, L.; Liang, C.; Liu, Q.; Zhu, G. Heterojunction of facet coupled g-C_3N_4/surface-fluorinated TiO_2 nanosheets for organic pollutants degradation under visible LED light irradiation. *Appl. Catal. B* **2014,** *156-157*, 331-340.
40. Lee, K.-M.; Chang, S. H.; Wu, M.-C.; Wu, C.-G. Raman and photoluminescence investigation of CdS/CdSe quantum dots on TiO_2 nanoparticles with multi-walled carbon nanotubes and their application in solar cells. *Vib. Spectrosc.* **2015,** *80*, 66-69.
41. Potlog, T.; Dobromir, M.; Luca, D.; Onufrijevs, P.; Medvids, A.; Shamardin, A. Rutile to anatase phase transition in TiO_2:Nb thin films by annealing in H_2 atmosphere. *Curr. Appl. Phys.* **2016,** *16*, 826-829.
42. Papailias, I.; Giannakopoulou, T.; Todorova, N.; Demotikali, D.; Vaimakis, T.; Trapalis, C. Effect of processing temperature on structure and photocatalytic properties of g-C_3N_4. *Appl. Surf. Sci.* **2015,** *358, Part A*, 278-286.
43. Jiang, J.; Ou-yang, L.; Zhu, L.; Zheng, A.; Zou, J.; Yi, X.; Tang, H. Dependence of electronic structure of g-C_3N_4 on the layer number of its nanosheets: A study by Raman spectroscopy coupled with first-principles calculations. *Carbon* **2014,** *80*, 213-221.
44. Shan, W.; Hu, Y.; Bai, Z.; Zheng, M.; Wei, C. In situ preparation of g-C_3N_4/bismuth-based oxide nanocomposites with enhanced photocatalytic activity. *Appl. Catal. B* **2016,** *188*, 1-12.
45. Yang, X.; Qian, F.; Zou, G.; Li, M.; Lu, J.; Li, Y.; Bao, M. Facile fabrication of acidified g-C_3N_4/g-C_3N_4 hybrids with enhanced photocatalysis performance under visible light irradiation. *Appl. Catal. B* **2016,** *193*, 22-35.
46. Sangchay, W.; Sikong, L.; Kooptarnond, K. Comparison of photocatalytic reaction of commercial P25 and synthetic TiO_2-AgCl nanoparticles. *Procedia Eng.* **2012,** *32*, 590-596.
47. Zhang, Y.; Pan, Q.; Chai, G.; Liang, M.; Dong, G.; Zhang, Q.; Qiu, J. Synthesis and luminescence mechanism of multicolor-emitting g-C_3N_4 nanopowders by low temperature thermal condensation of melamine. *Sci. Rep.* **2013,** *3*, 1-8.
48. Li, X.; Zhang, J.; Shen, L.; Ma, Y.; Lei, W.; Cui, Q.; Zou, G. Preparation and characterization of graphitic carbon nitride through pyrolysis of melamine. *Appl. Phys. A* **2009,** *94*, 387-392.
49. Fu, M.; Pi, J.; Dong, F.; Duan, Q.; Guo, H. A cost-effective solid-state approach to aynthesize g-C_3N_4 coated TiO_2 nanocomposites with enhanced visible light photocatalytic activity. *Int. J. Photoenergy* **2013,** *2013*, 1-7.
50. Ma, J.; Wang, C.; He, H. Enhanced photocatalytic oxidation of NO over g-C_3N_4-TiO_2 under UV and visible light. *Appl. Catal. B* **2016,** *184*, 28-34.
51. Jo, W.-K.; Natarajan, T. S. Influence of TiO_2 morphology on the photocatalytic efficiency of direct Z-scheme g-C_3N_4/TiO_2 photocatalysts for isoniazid degradation. *Chem. Eng. J.* **2015,** *281*, 549-565.
52. Xiao, H.; Wang, W.; Liu, G.; Chen, Z.; Lv, K.; Zhu, J. Photocatalytic performances of g-C_3N_4 based catalysts for RhB degradation: Effect of preparation conditions. *Appl. Surf. Sci.* **2015,** *358, Part A*, 313-318.
53. Wang, S.; Li, C.; Wang, T.; Zhang, P.; Li, A.; Gong, J. Controllable synthesis of nanotube-type graphitic C_3N_4 and their visible-light photocatalytic and fluorescent properties. *J. Mater. Chem. A* **2014,** *2*, 2885-2890.
54. Wang, X.; Zhang, L.; Lin, H.; Nong, Q.; Wu, Y.; Wu, T.; He, Y. Synthesis and characterization of a ZrO_2/g-C_3N_4 composite with enhanced visible-light photoactivity for rhodamine degradation. *RSC Adv.* **2014,** *4*, 40029-40035.

55. Song, Z.; Hrbek, J.; Osgood, R. Formation of TiO_2 nanoparticles by reactive-layer-assisted deposition and characterization by XPS and STM. *Nano Lett.* **2005,** *5*, 1327-1332.
56. Li, H.; Li, J.; Huo, Y. Highly active TiO_2N photocatalysts prepared by treating TiO_2 precursors in NH_3/ethanol fluid under supercritical conditions. *J. Phys. Chem. B* **2006,** *110*, 1559-1565.
57. Ola, O.; Maroto-Valer, M. M. Review of material design and reactor engineering on TiO_2 photocatalysis for CO_2 reduction. *J. Photochem. Photobiol. C* **2015,** *24*, 16-42.
58. Ohtani, B. Photocatalysis A to Z—what we know and what we do not know in a scientific sense. *J. Photochem. Photobiol. C* **2010,** *11*, 157-178.
59. Bai, S.; Jiang, J.; Zhang, Q.; Xiong, Y. Steering charge kinetics in photocatalysis: intersection of materials syntheses, characterization techniques and theoretical simulations. *Chem. Soc. Rev.* **2015,** *44*, 2893-2939.
60. Li, J.; Liu, Y.; Li, H.; Chen, C. Fabrication of g-C_3N_4/TiO_2 composite photocatalyst with extended absorption wavelength range and enhanced photocatalytic performance. *J. Photochem. Photobiol. A* **2016,** *317*, 151-160.

Table of contents image:

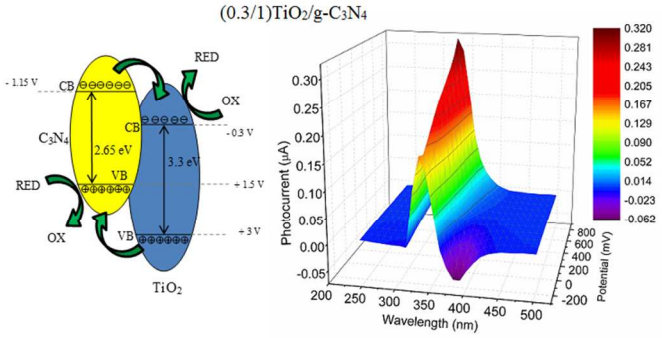

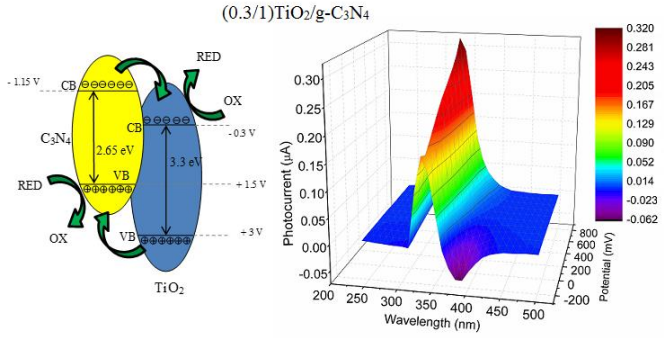
(0.3/1)TiO2/g-C3N4
- 1.15 V
CB
RED
OX
CB
- 0.3 V
C3N4
2.65 eV
3.3 eV
VB
RED
+ 1.5 V
OX
VB
+ 3 V
TiO2
Photocurrent (μA)
0.30
0.25
0.20
0.15
0.10
0.05
0.00
-0.05
200
250
300
350
400
450
500
Wavelength (nm)
800
600
400
200
0
-200
Potential (mV)
0.320
0.281
0.243
0.205
0.167
0.129
0.090
0.052
0.014
-0.023
-0.062

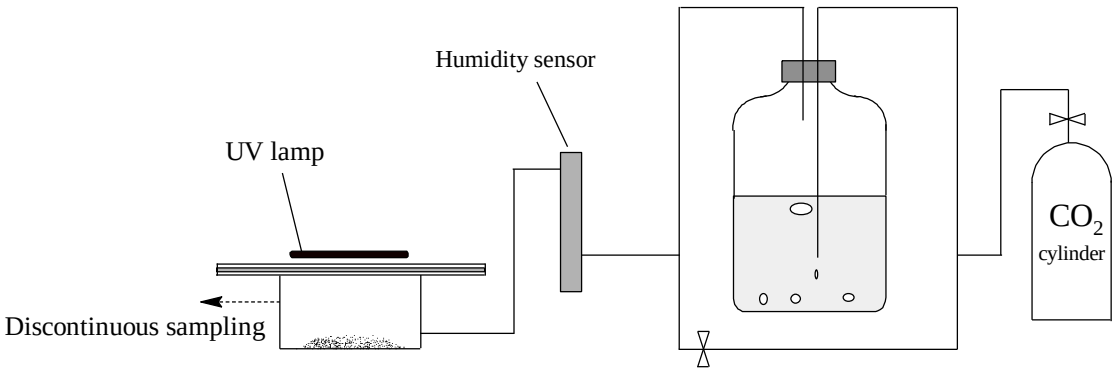
Humidity sensor
UV lamp
Discontinuous sampling
CO_2
cylinder

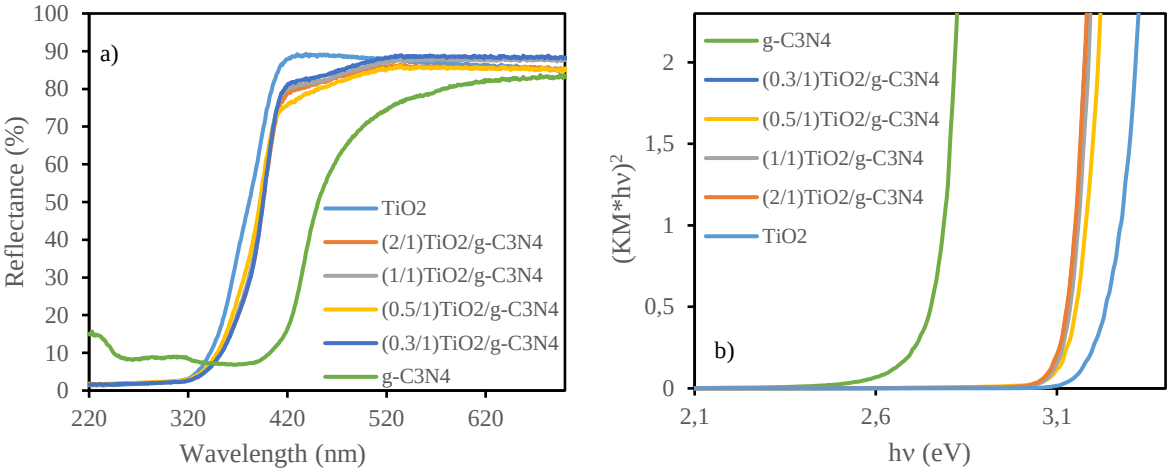
a)
Reflectance (%)
Wavelength (nm)
100
90
80
70
60
50
40
30
20
10
0
220
320
420
520
620
TiO2
(2/1)TiO2/g-C3N4
(1/1)TiO2/g-C3N4
(0.5/1)TiO2/g-C3N4
(0.3/1)TiO2/g-C3N4
g-C3N4
b)
(KM*hν)²
hν (eV)
2
1,5
1
0,5
0
2,1
2,6
3,1
g-C3N4
(0.3/1)TiO2/g-C3N4
(0.5/1)TiO2/g-C3N4
(1/1)TiO2/g-C3N4
(2/1)TiO2/g-C3N4
TiO2

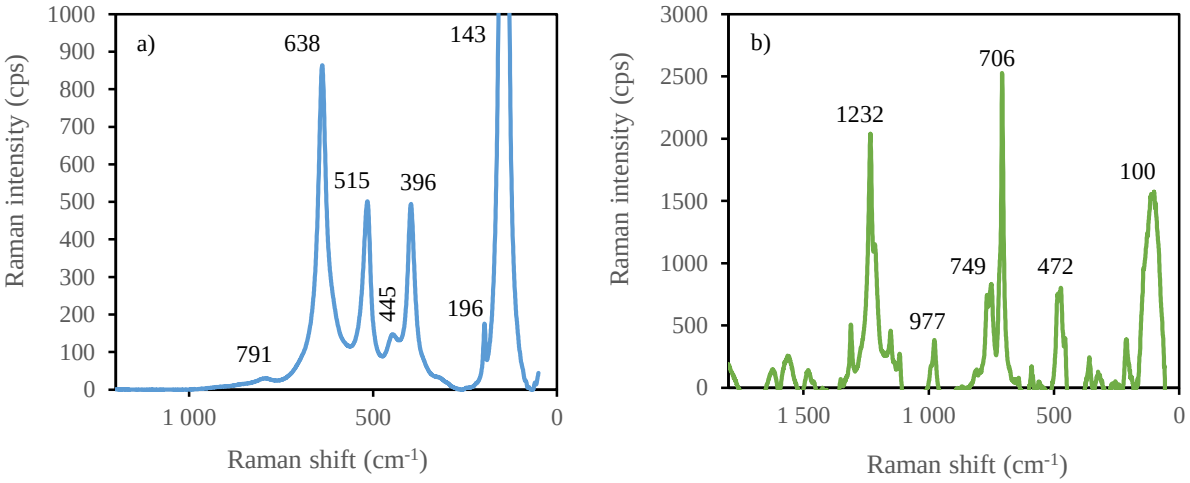
a)
638
143
515
396
445
196
791
Raman intensity (cps)
Raman shift (cm-1)
b)
706
1232
100
749
472
977
Raman intensity (cps)
Raman shift (cm-1)

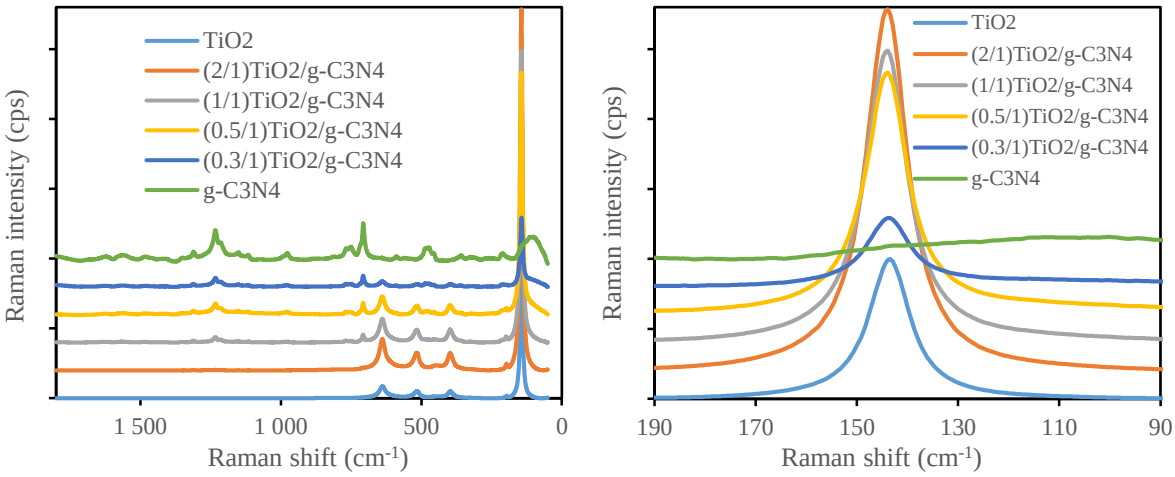
TiO2
(2/1)TiO2/g-C3N4
(1/1)TiO2/g-C3N4
(0.5/1)TiO2/g-C3N4
(0.3/1)TiO2/g-C3N4
g-C3N4
Raman intensity (cps)
1 500
1 000
500
0
Raman shift (cm-1)
190
170
150
130
110
90

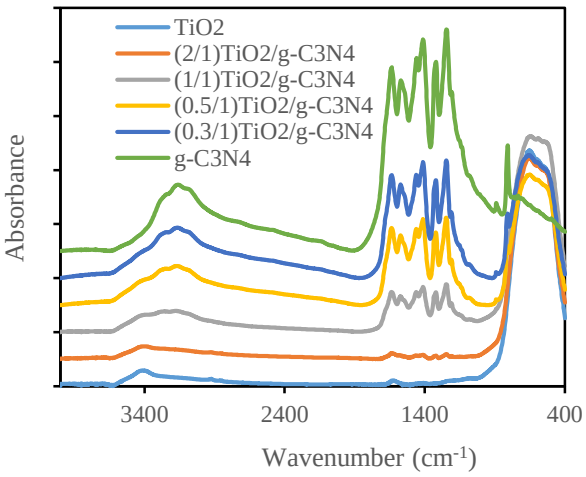
TiO2
(2/1)TiO2/g-C3N4
(1/1)TiO2/g-C3N4
(0.5/1)TiO2/g-C3N4
(0.3/1)TiO2/g-C3N4
g-C3N4
Absorbance
3400
2400
1400
400
Wavenumber (cm-1)

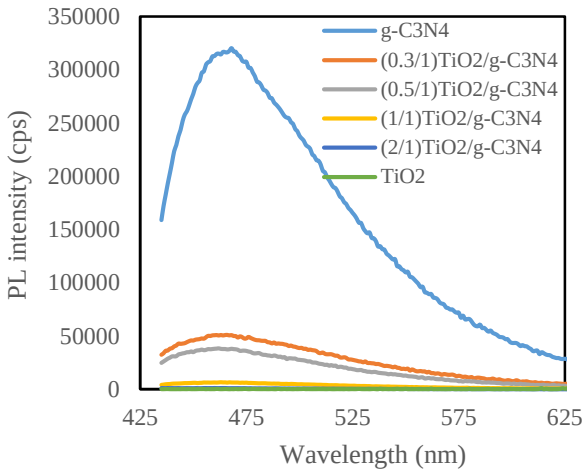
350000
300000
250000
200000
150000
100000
50000
0
PL intensity (cps)
425
475
525
575
625
Wavelength (nm)
g-C3N4
(0.3/1)TiO2/g-C3N4
(0.5/1)TiO2/g-C3N4
(1/1)TiO2/g-C3N4
(2/1)TiO2/g-C3N4
TiO2

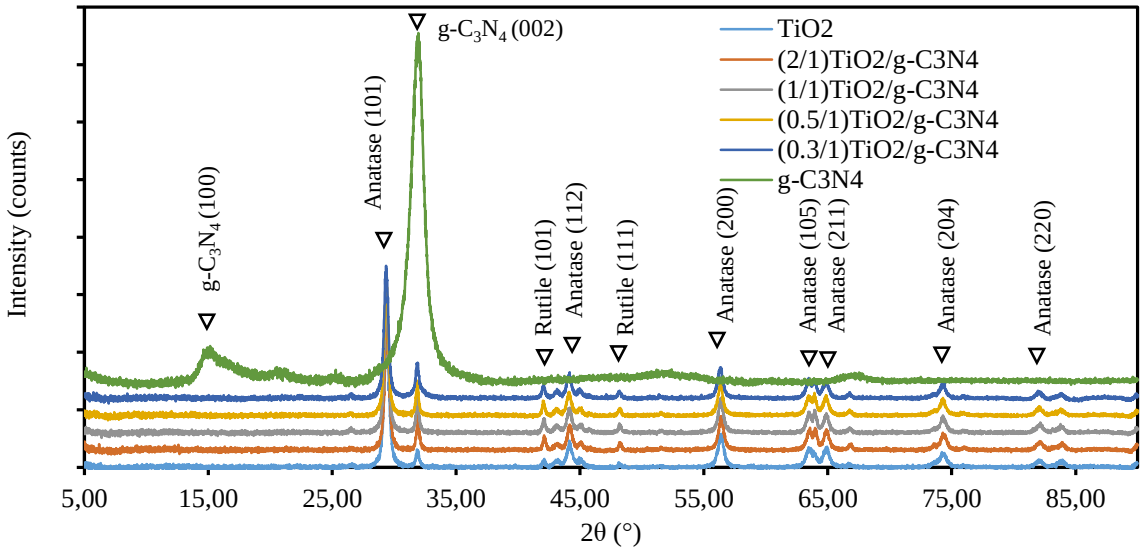
Intensity (counts)
2θ (°)
5,00
15,00
25,00
35,00
45,00
55,00
65,00
75,00
85,00
g-C3N4 (100)
Anatase (101)
g-C3N4 (002)
Rutile (101)
Anatase (112)
Rutile (111)
Anatase (200)
Anatase (105)
Anatase (211)
Anatase (204)
Anatase (220)
TiO2
(2/1)TiO2/g-C3N4
(1/1)TiO2/g-C3N4
(0.5/1)TiO2/g-C3N4
(0.3/1)TiO2/g-C3N4
g-C3N4

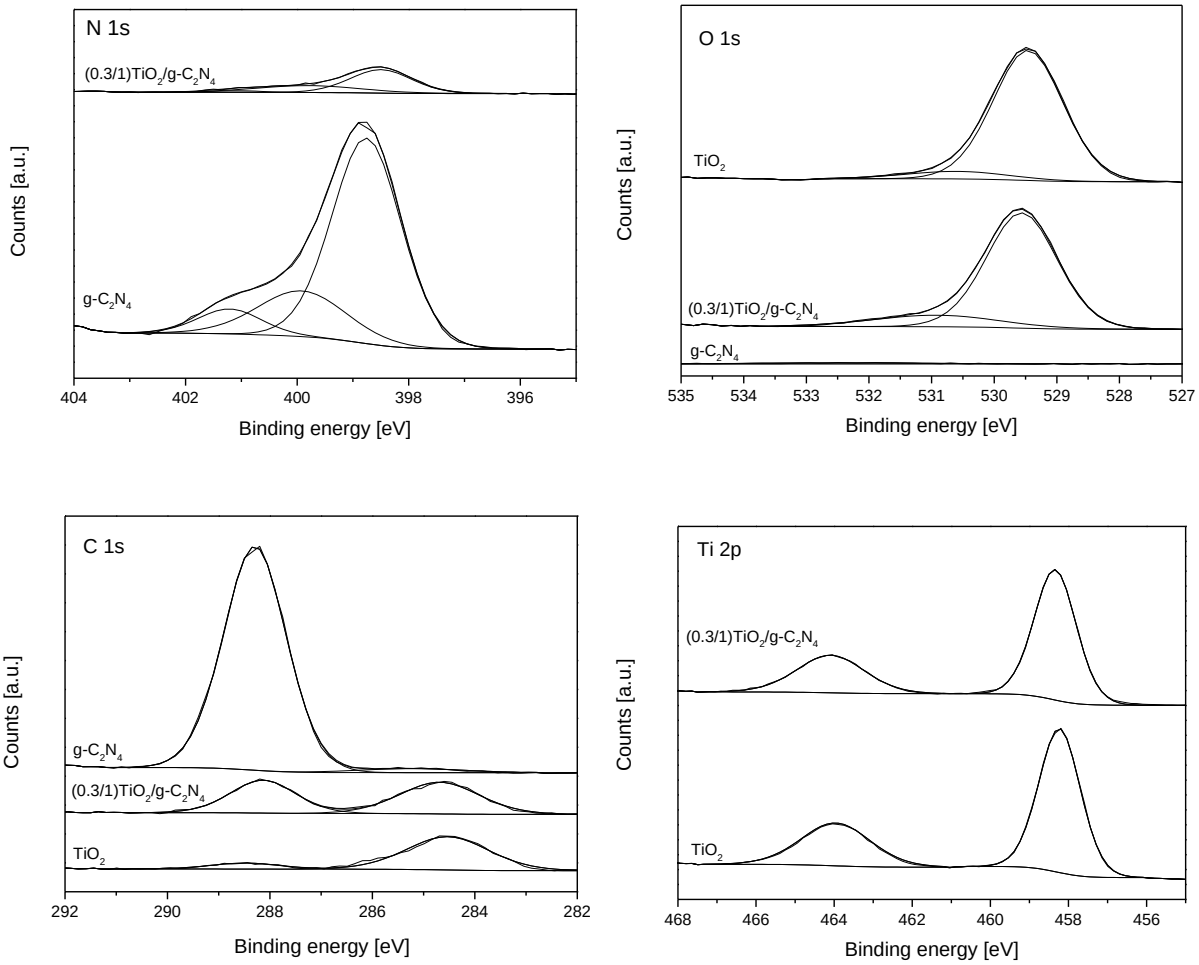
N 1s
(0.3/1)TiO2/g-C2N4
g-C2N4
Counts [a.u.]
404
402
400
398
396
Binding energy [eV]
O 1s
TiO2
(0.3/1)TiO2/g-C2N4
g-C2N4
Counts [a.u.]
535
534
533
532
531
530
529
528
527
Binding energy [eV]
C 1s
g-C2N4
(0.3/1)TiO2/g-C2N4
TiO2
Counts [a.u.]
292
290
288
286
284
282
Binding energy [eV]
Ti 2p
(0.3/1)TiO2/g-C2N4
TiO2
Counts [a.u.]
468
466
464
462
460
458
456
Binding energy [eV]

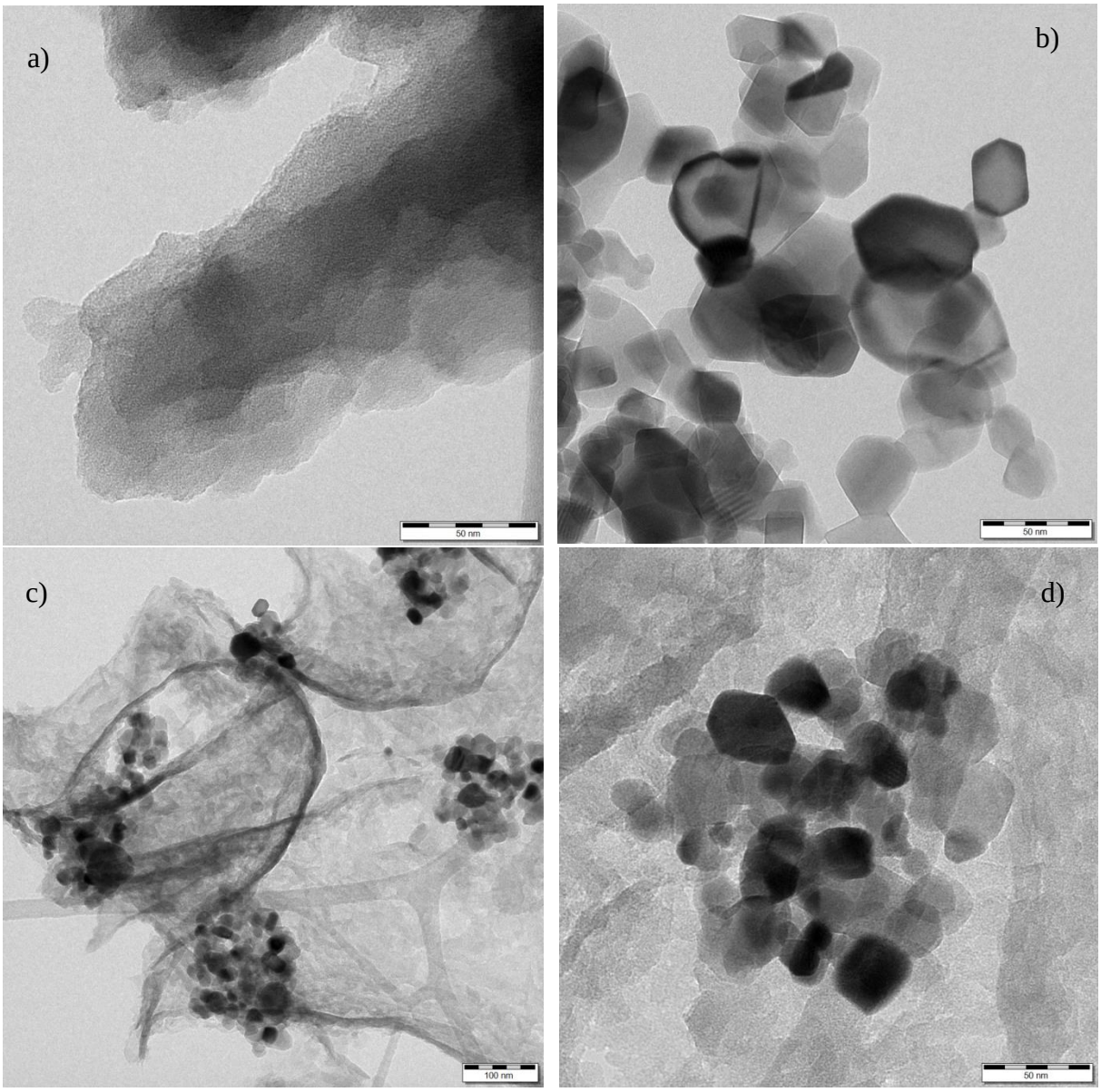
a)
50 nm
b)
50 nm
c)
100 nm
d)
50 nm

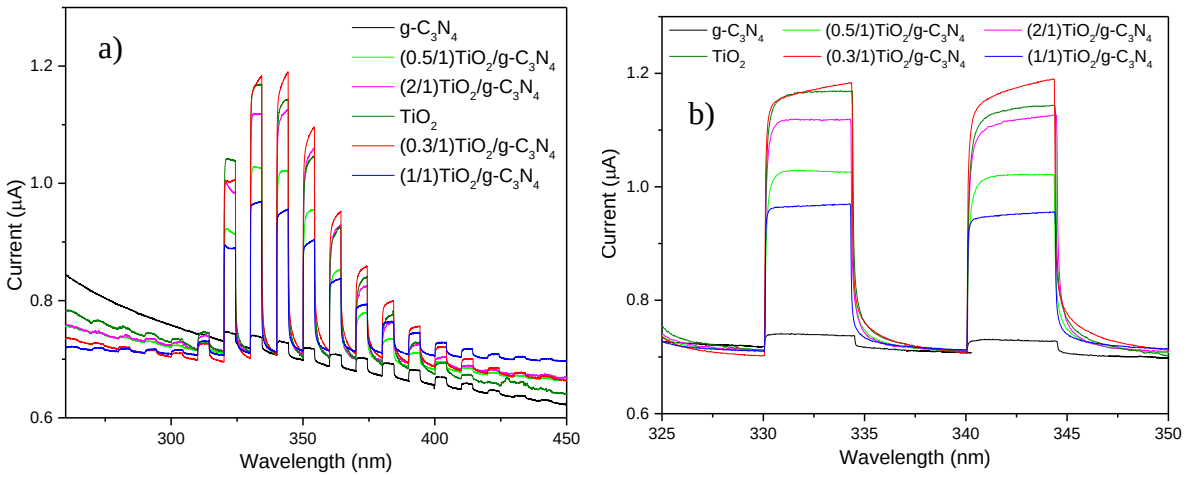
a)
g-C3N4
(0.5/1)TiO2/g-C3N4
(2/1)TiO2/g-C3N4
TiO2
(0.3/1)TiO2/g-C3N4
(1/1)TiO2/g-C3N4
Current (μA)
Wavelength (nm)
b)
g-C3N4
(0.5/1)TiO2/g-C3N4
(2/1)TiO2/g-C3N4
TiO2
(0.3/1)TiO2/g-C3N4
(1/1)TiO2/g-C3N4
Current (μA)
Wavelength (nm)

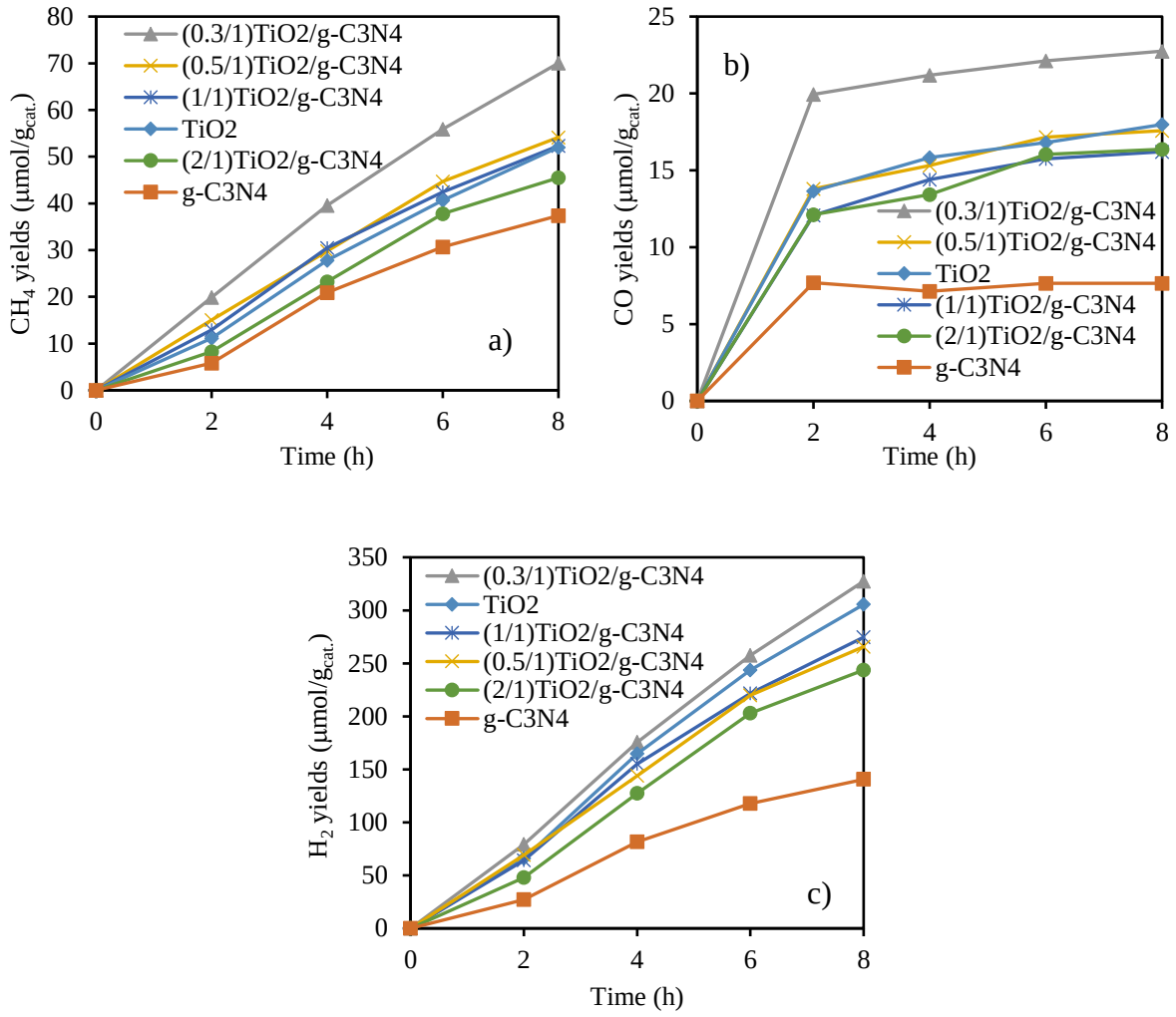
(0.3/1)TiO2/g-C3N4
(0.5/1)TiO2/g-C3N4
(1/1)TiO2/g-C3N4
TiO2
(2/1)TiO2/g-C3N4
g-C3N4
CH4 yields (μmol/gcat.)
Time (h)
a)
CO yields (μmol/gcat.)
b)
H2 yields (μmol/gcat.)
c)

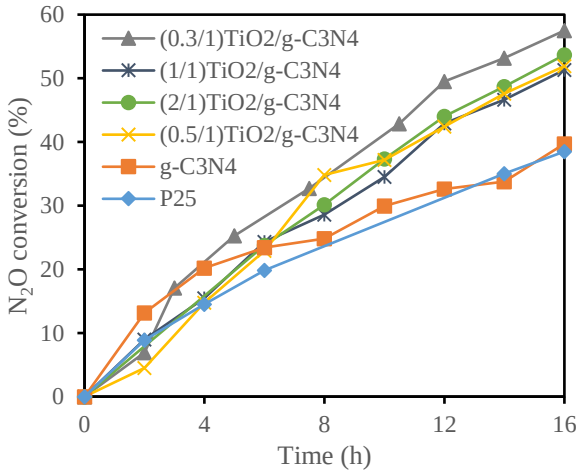
60
50
40
30
20
10
0
0
4
8
12
16
Time (h)
N2O conversion (%)
(0.3/1)TiO2/g-C3N4
(1/1)TiO2/g-C3N4
(2/1)TiO2/g-C3N4
(0.5/1)TiO2/g-C3N4
g-C3N4
P25

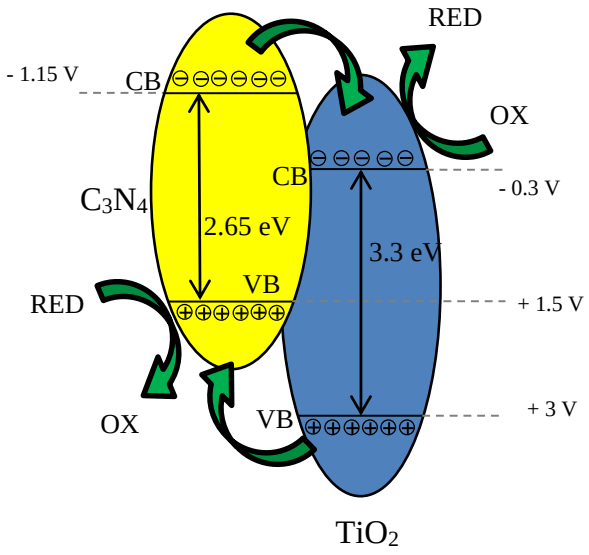
RED
OX
- 1.15 V
CB
CB
- 0.3 V
C_3N_4
2.65 eV
3.3 eV
VB
RED
+ 1.5 V
OX
VB
+ 3 V
TiO_2